

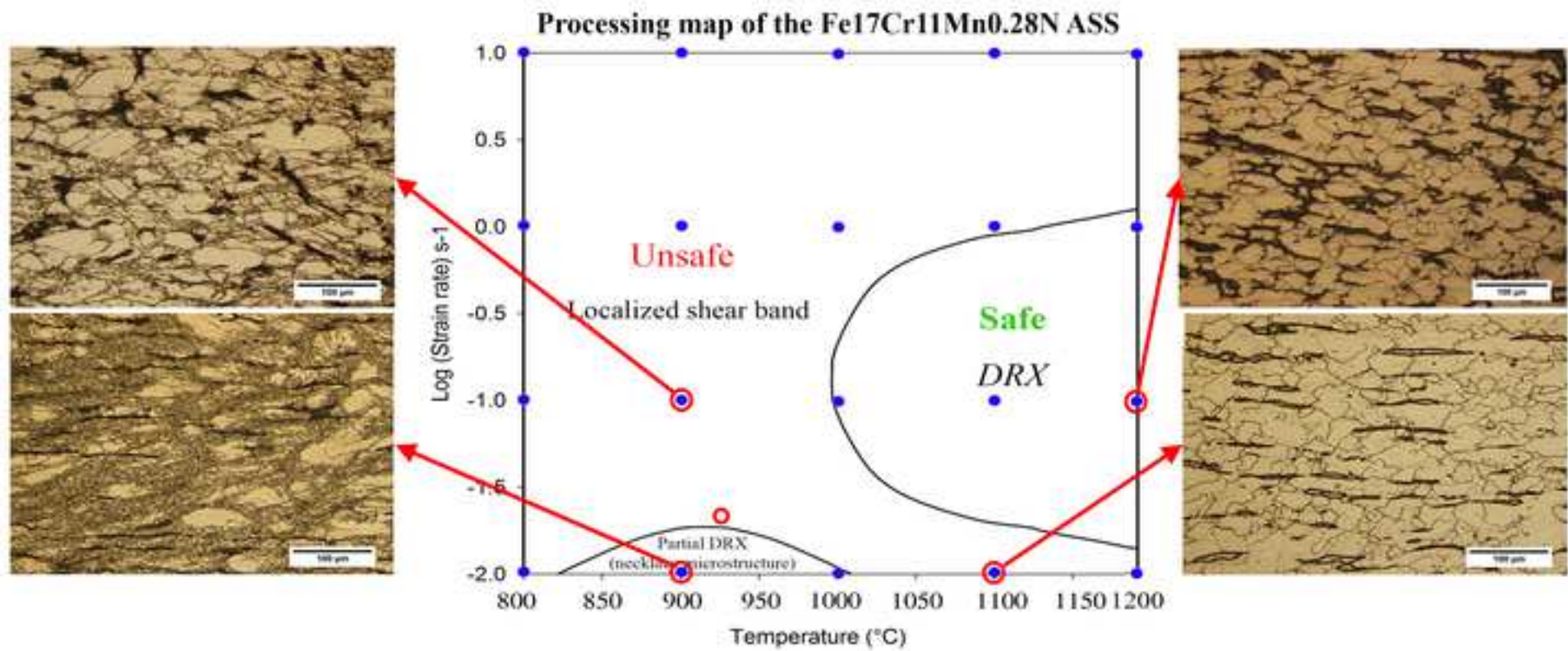
Materials Today Communications

Design of a hot deformation processing map for a Ni-free, N-bearing austenitic stainless steel --Manuscript Draft--

Manuscript Number:	MTCOMM-D-21-00264R1
Article Type:	Full Length Article
Section/Category:	Mechanical properties
Keywords:	Hot deformation; Ni-free austenitic stainless steel; Processing Map; DRX; Instability
Corresponding Author:	Ahmad Kermanpur Isfahan Univ. Tech. Isfahan, Iran IRAN, ISLAMIC REPUBLIC OF
First Author:	H. Khorshidi
Order of Authors:	H. Khorshidi Ahmad Kermanpur, Ph.D. H. Rastegari E. Ghassemali M.C. Somani
Abstract:	<p>The hot deformation characteristics of a FeCrMnN austenitic stainless steel containing 0.28 wt.% nitrogen (N) was investigated by hot compression tests using a Gleeble simulator in the temperature range of 800-1200°C and at constant true strain rates of 0.01 to 10 s⁻¹ with all specimens deformed to ~0.9 true strain. The influence of deformation conditions on microstructural mechanisms and phase transformations was characterized. A processing map based on dynamic materials modelling (DMM) was designed and interpreted for predicting the domain of stable flow for safe, defect-free hot deformation. The results revealed the occurrence of dynamic recrystallization (DRX) in a domain extending over the temperature and strain rate ranges of 1100-1200°C and 0.1-1 s⁻¹, respectively, with the efficiency of power dissipation (η) of 45-55 %. Decreasing temperature and increasing strain rate led to a reduction in DRX grain size following microstructural reconstitution. Another small deterministic domain of 820-1000°C and 0.01-0.05 s⁻¹ was identified showing occurrence of partial DRX in shear bands leading to formation of a mixed microstructure. The instability criteria delineated the regime of unstable flow covering a large part of the processing map extending over low temperatures (800-950°C) and high strain rates (0.1-10 s⁻¹) that must be avoided during processing.</p>
Suggested Reviewers:	Young Kook Lee ykleee@yonsei.ac.kr Abbas Najafizadeh abbas.najafizadeh@gmail.com David Porter david.porter@oulu.fi John Josef Jonas john.jonas@mcgill.ca
Opposed Reviewers:	
Response to Reviewers:	

Highlights

- Hot deformation processing map of a FeCrMnN stainless steel was designed.
- Dynamic recrystallization occurred in temperature of 1100-1200 °C and strain rate of 0.1-1 s⁻¹.
- Decreasing temperature and increasing strain rate reduced dynamically recrystallized grain size.
- Unstable flow may occur at temperatures 800-950 °C and strain rates 0.1-10 s⁻¹.



Design of a hot deformation processing map for a Ni-free, N-bearing austenitic stainless steel

H. Khorshidi^a, A. Kermanpur^{a,1}, H. Rastegari^b, E. Ghassemali^c and M.C. Somani^d

^a *Department of Materials Engineering, Isfahan University of Technology, Isfahan 84156-83111, Iran*

^b *Department of Mechanical and Materials Engineering, Birjand University of Technology, South Khorasan 97198-66981, Iran*

^c *Department of Materials and Manufacturing, School of Engineering, Jönköping University, Jönköping, Sweden*

^d *Centre for Advanced Steels Research, University of Oulu, P.O. Box 4200, 90014 Oulu, Finland*

Abstract

The hot deformation characteristics of a FeCrMnN austenitic stainless steel containing 0.28 wt.% **nitrogen (N)** was investigated by hot compression tests using a Gleeble simulator in the temperature range of 800-1200°C and at constant true strain rates of 0.01 to 10 s⁻¹ with all specimens deformed to ~0.9 true strain. The influence of deformation conditions on microstructural mechanisms and phase transformations was characterized. A processing map based on dynamic materials modelling (DMM) was designed and interpreted for predicting the domain of stable flow for safe, defect-free hot deformation. The results revealed the occurrence of dynamic recrystallization (DRX) in a domain extending over the temperature and strain rate ranges of 1100-1200°C and 0.1-1 s⁻¹, respectively, with the efficiency of power dissipation (η) of 45-55 %. Decreasing temperature and increasing strain rate led to a reduction in DRX grain size following microstructural reconstitution. Another small deterministic domain of 820-1000°C and 0.01-0.05 s⁻¹ was identified showing occurrence of partial DRX in shear bands leading to formation of a mixed microstructure. The instability criteria delineated the regime of unstable flow covering a large part of the processing map extending over low temperatures (800-950°C) and high strain rates (0.1-10 s⁻¹) that must be avoided during processing.

Keywords

Hot deformation; Ni-free austenitic stainless steel; Processing map; DRX; Instability.

¹ Corresponding author. Tel.: (+9831) 3391 5738 ; Fax: (+9831) 3391 2752; E-mail: ahmad_k@iut.ac.ir (A. Kermanpur)

1. Introduction

In recent years, nitrogen (N) has been used in austenitic stainless steels (ASSs), leading to a reduction and even complete elimination of nickel (Ni) as the austenite stabilizing element [1-3]. Besides the advantage of lowering the steel cost, replacing Ni completely with N in the steel also solves the allergy-related problems caused by Ni ions on human skin. Various sources in literature confirm that adding N to ASSs improves both mechanical as well as corrosion properties [4-7]. Kim et al. reported that increasing N in ASSs increased the yield strength and ultimate tensile strength [4]. Ha et al. investigated Fe-Cr-Mn-(0.39-0.69) N steels and showed an improvement in pitting corrosion resistant due to the presence of an increased content of N [7].

Structural changes of stainless steels during thermomechanical processing are very important due to their effect on excellent corrosion resistance properties and mechanical properties of these steels. It is reported that the dynamic recrystallization (DRX) during hot deformation of the ASSs occurs by bulging mechanism and growth of a necklace structure [8-11]. The occurrence of changes in the microstructure such as texture formation, precipitation and grain boundary distribution during hot deformation have been suitably assessed by relevant structural examination techniques [12-14]. Several constitutive equations have since been derived for the modeling of hot deformation and flow curves with the Zener-Hollomon (Z) parameter based on general relations or modified Arrhenius type equations proposed by Yang et al [15-19]. A processing map is used to evaluate the hot deformation behavior in temperature - strain rate space and provides an opportunity for the estimation of optimal hot or warm working conditions based on the principles of the dynamic materials modelling (DMM) [20-23]. In this model, a workpiece undergoing hot deformation is considered to be a dissipator of power. At any instant, the dissipation of total input power (P) occurs through a temperature rise (G

content) and a microstructural change (*J co-content*) and the partitioning of power between G and J at any given temperature and strain is determined by the strain rate sensitivity (m) of the flow stress (σ). At a given temperature and strain, the *J co-content* is given by [23, 24]:

$$J = [m/(m+1)] \cdot \sigma \dot{\epsilon} \quad (1)$$

where $\dot{\epsilon}$ is the strain rate. The *J co-content* of the workpiece, which is a non-linear dissipator, is normalized with that of an ideal dissipator ($m = 1$) to obtain a dimensionless parameter called the efficiency of power dissipation (η):

$$\eta = \frac{J}{J_{max}} = \frac{2m}{m+1} \quad (2)$$

This parameter (η) helps in mapping the dissipative microstructural characteristics of the workpiece and when plotted in a wide range of temperature and strain rate, constitutes the power dissipation map. Based on the principles of irreversible thermodynamics applied to large plastic flow, an instability parameter ($\xi(\dot{\epsilon})$) has also been developed [23, 24], which suggests manifestation of metallurgical flow instability during hot deformation, if $\xi(\dot{\epsilon})$ parameter (Equation 3) becomes negative:

$$\xi(\dot{\epsilon}) = \frac{\partial \ln(m/m+1)}{\partial \ln \dot{\epsilon}} + m \quad (3)$$

The variation of ($\xi(\dot{\epsilon})$) parameter over a broad range of temperature and strain rate constitutes an instability map. A processing map is generated by superimposing the flow instability map on the power dissipation map, thus delineating the regime/s of flow instabilities.

Although the hot deformation behavior of ASSs including Ni-free variants with high N content have been widely investigated, less attention has been paid to the ASSs with low N content (<0.3 wt.%). The objective of the present investigation is to develop a processing map to characterize the constitutive hot deformation behavior of a Ni-free ASS containing ~0.3 wt. %

N utilizing uniaxial hot compression testing carried out over broad temperature and strain rate ranges.

2. Materials and Experimental Procedures

The Ni-free ASS used in this steel was melted in a vacuum induction melting (VIM) furnace of ~10 kg capacity. The molten steel was maintained under a pressure of 150 mbar N₂ gas to add N to the steel melt. The cast ingot was then refined by an electro-slag refining (ESR) system leading to the final chemical composition of 17.1 %Cr, 11.3 %Mn, 0.27 %Si, 0.28 %N, 0.06 %C and 0.004 % Mo (in wt. %). The ESRed material was then homogenized at 1200 °C for 5 h followed by hot forging at 1100 °C. The as-forged samples were subjected to stress-relief annealing at 1000 °C for 1 h. Cylindrical test specimens of the dimensions ϕ 6 mm \times 9 mm were machined out of the forged sample and hot compression tests were performed using the Gleeble 3800 thermomechanical simulator over a wide matrix of temperature and strain rate ranges of 800-1200 °C and 0.01-10 s⁻¹, respectively, to a true strain of about 1.0. A graphite foil and a tantalum foil were used between the test cylinders and the tungsten carbide anvils in order to reduce friction during the hot compression tests. The tantalum foils also prevented excessive heating of the anvils. The experimental scheme of the hot deformation tests is shown in Fig. 1.

The microstructural investigation was conducted by light optical microscopy (LOM) technique. The samples were electro-etched with 65% HNO₃ solution at a voltage of 1.2 V for 60 s. A field emission scanning electron microscope (FESEM, TESCAN JEOL JSM7001F) equipped with the electron backscatter diffraction (EBSD) facility was employed for detailed microstructural characterization at high magnifications. The EBSD samples were prepared by mechanical polishing with 0.1 micrometer alumina powder followed by electro-polishing with a solution containing 10% perchloric acid and 90% ethanol using a potential of 10 V d.c. for 120-190 s at ambient temperature. The phase identification was carried out by X-ray diffraction

(XRD; Phillips Expert MPD) using a Cu-K α radiation ($10^\circ < 2\theta < 100^\circ$, 40 kV, 30 mA) at room temperature. Thermodynamic calculations were performed using the Thermo-Calc® software with the TCFE7 steel database. The variation of phase fraction as a function of temperature for the studied steel is shown in Fig. 2.

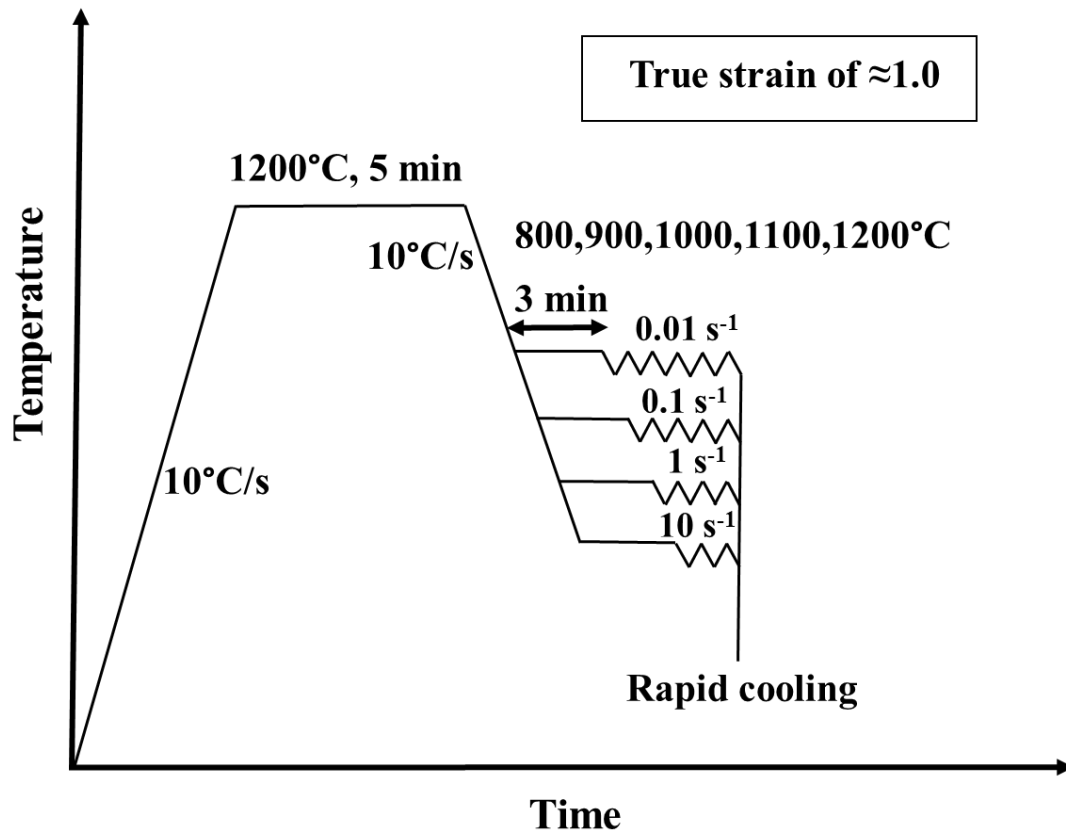


Fig. 1. Experimental scheme of the hot deformation process.

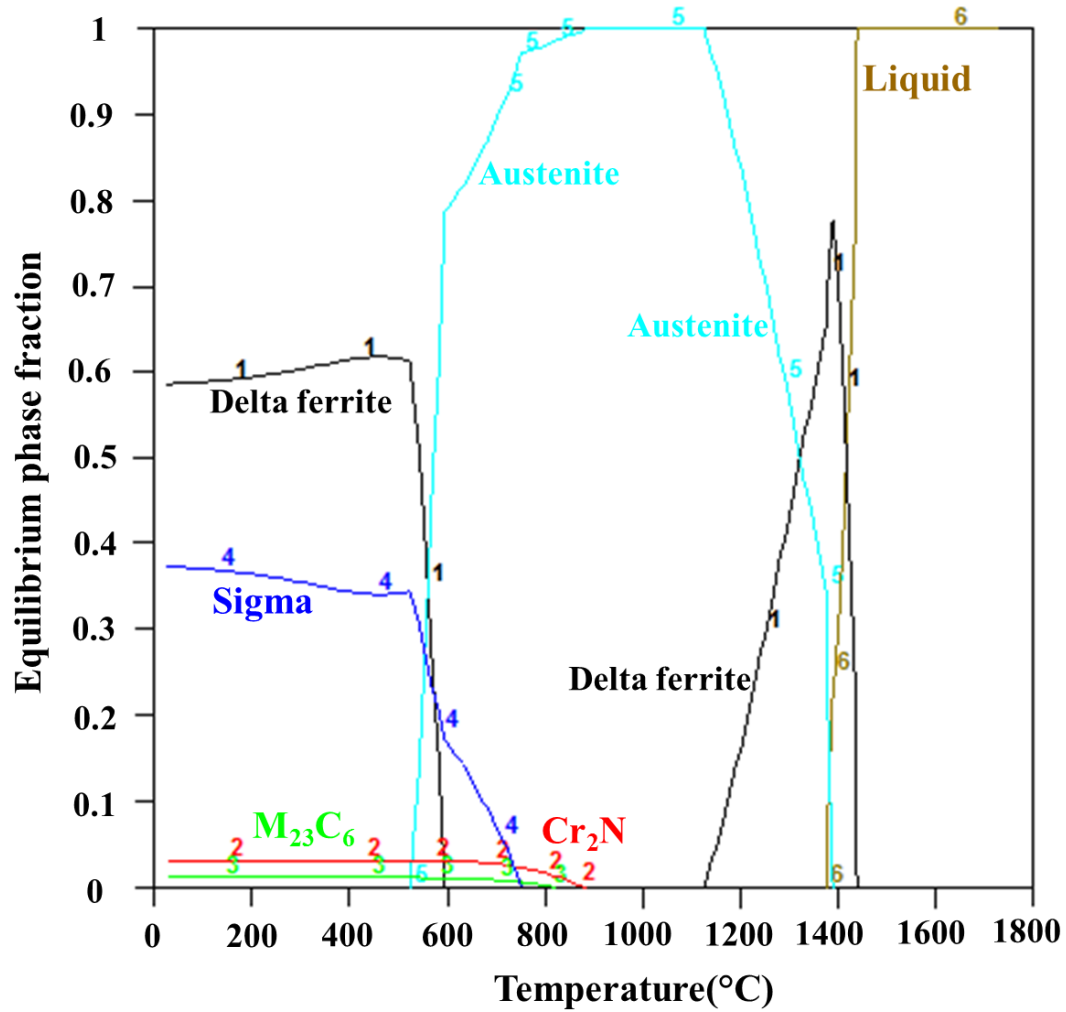


Fig. 2. The variation of phase fraction vs. temperature predicted from thermodynamic calculations using the Thermo-Calc® software with TCFE7 database.

3. Results and discussion

3.1. Initial microstructures

The LOM image and XRD pattern of the annealed steel are shown in Fig. 3. The steel displayed essentially austenitic microstructure along with the presence of approximately 6% delta ferrite (dark area in Fig. 3 a). The average grain size using the linear intercept method was estimated at approximately 55 μm with a wide size distribution as shown in Fig. 3 c.

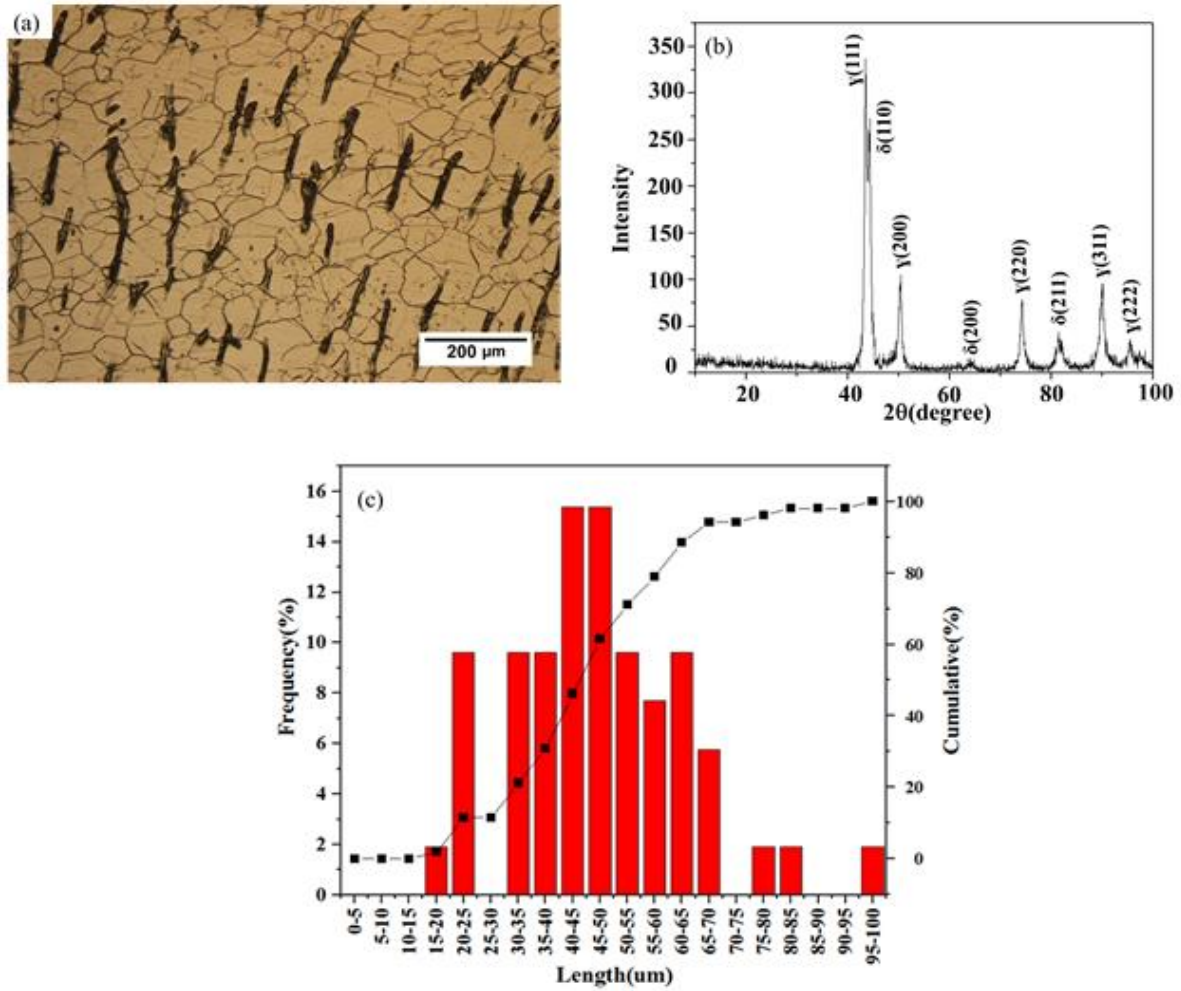


Fig. 3. The optical microstructure (a), XRD spectrum (b), and the histogram presenting the grain size distribution of the hot forged and annealed steel (c).

An important point concerning the hot deformation of N-containing stainless steels is the avoidance of deformation at temperatures leading to the strain-induced formation of harmful Cr_2N precipitation. The kinetics of Cr_2N precipitation has been analyzed at different temperatures as a function of time [25]. According to Fig. 4, it can be observed that the formation of Cr_2N precipitates under the selected deformation conditions was insignificant, though the rate of strain induced precipitation can be significantly higher.

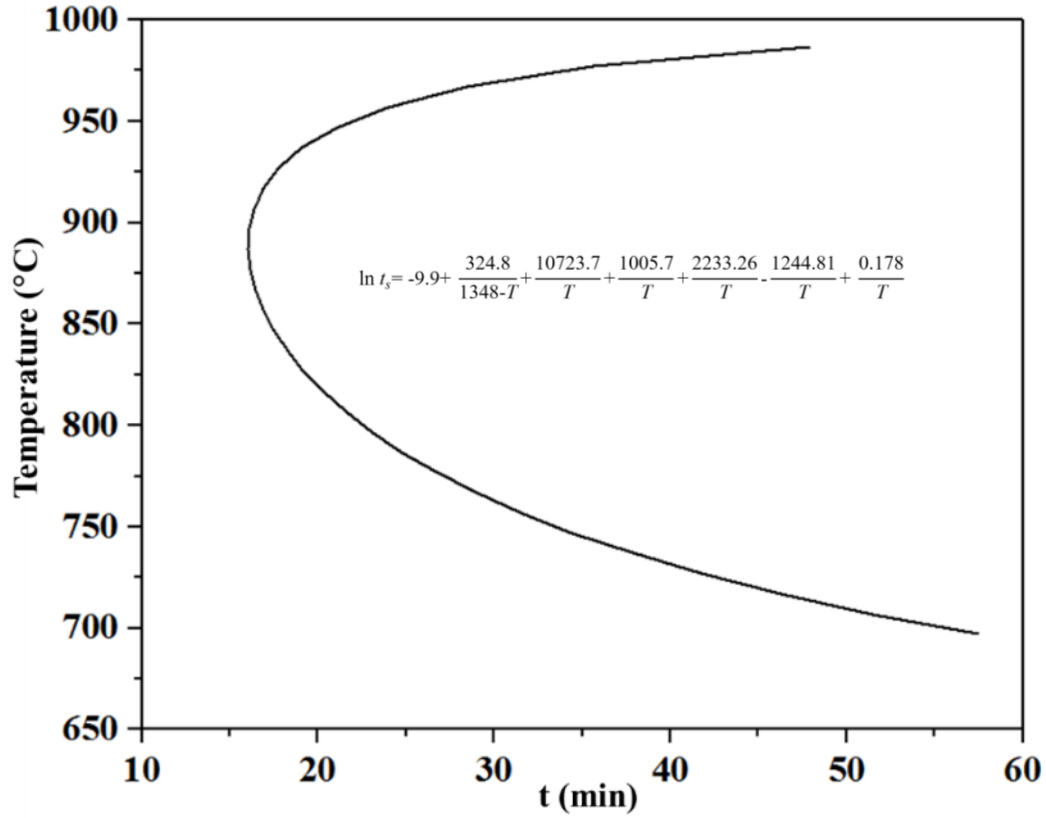


Fig. 4. The kinetics of Cr₂N formation in the investigated steel.

3.2. The hot deformation characteristics

The stress-strain curves obtained by hot compression tests under various deformation conditions are shown in Fig. 5. Evidently, under the influence of different temperature and strain rate conditions, the flow stress invariably changed such that at a higher temperature and lower strain rate, a lower flow stress was achieved, for instance. Under most deformation conditions, critical conditions marking the initiation of DRX were achieved, while dynamic recovery (DRV) occurred at the conditions of high strain rate and low temperatures, such as 800 °C/10 s⁻¹ and 900 °C/10 s⁻¹.

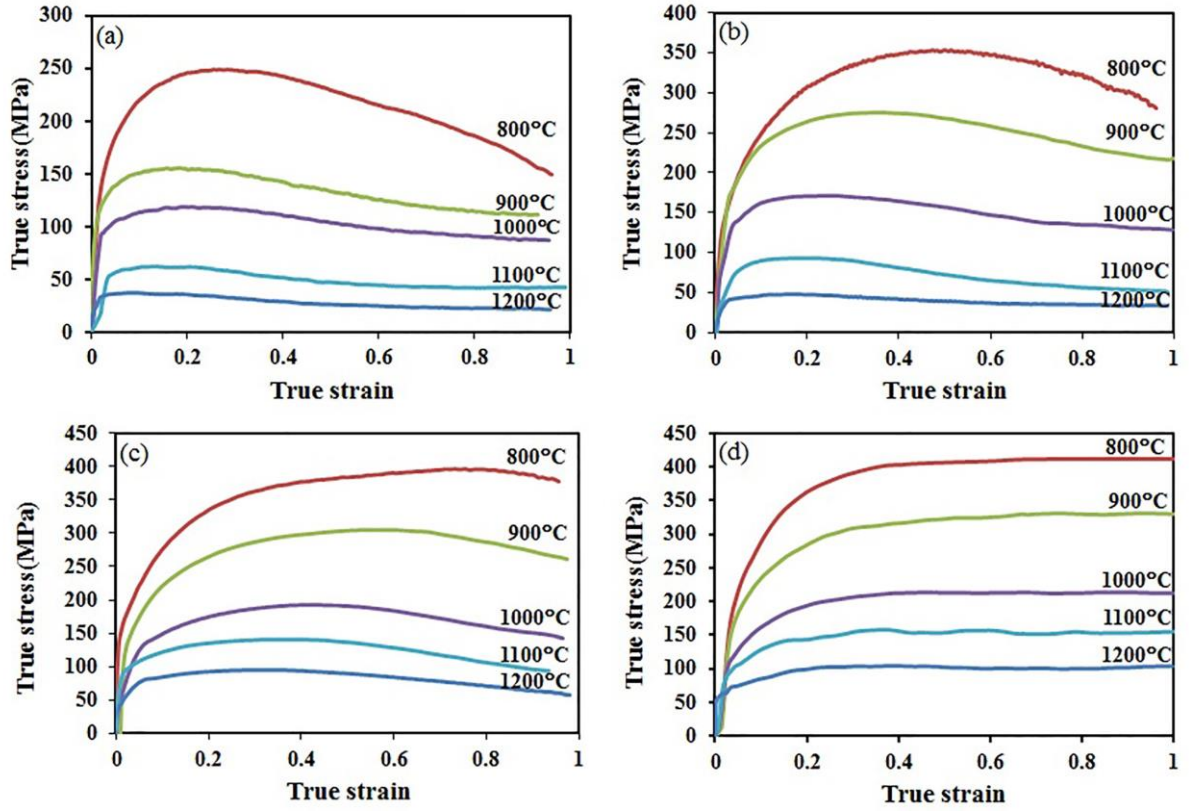


Fig. 5. The flow stress curves obtained for different conditions of deformation temperatures and strain rates of (a) 0.01 s^{-1} , (b) 0.1 s^{-1} , (c) 1 s^{-1} and (d) 10 s^{-1} .

Based on our study [26] the **Z parameter** for the steel under investigation can be described as:

$$Z = \dot{\epsilon} \exp\left(\frac{502000}{RT}\right) = 2.75 \times 10^{19} \{ \sinh(0.0065\sigma_P) \}^{6.12} \quad (4)$$

Or

$$\dot{\epsilon} = 2.75 \times 10^{19} \{ \sinh(0.0065\sigma_P) \}^{6.12} \exp\left(\frac{-502000}{RT}\right) \quad (5)$$

Where T, σ_P and R, are temperature (K), peak stress and Gas constant, respectively. The average values of material constants (A, n and α) were calculated through a linear regression analysis [26]. The critical stress and strain were determined using work hardening rate (θ) calculations, which showed the changes in the slopes of the curves, as plotted in Fig. 6, representing the onset of recrystallization.

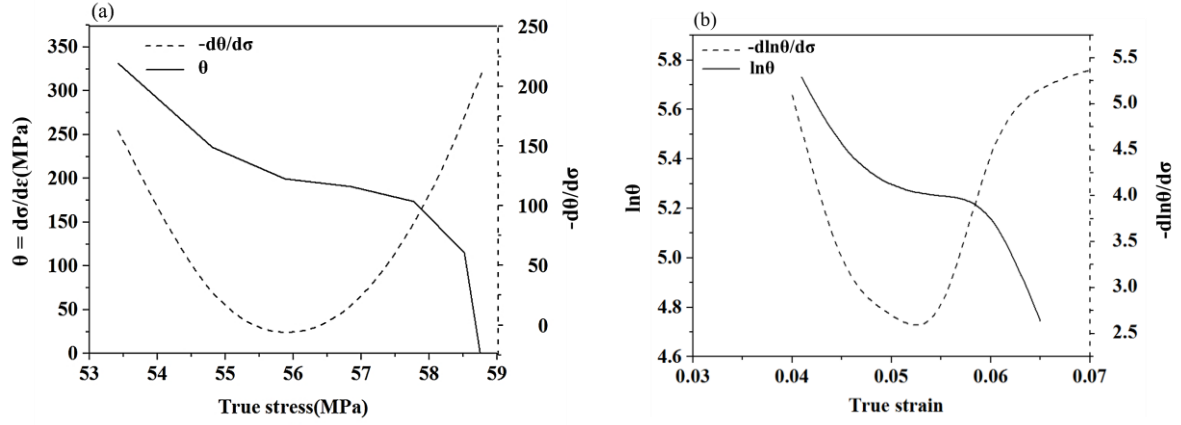


Fig. 6. Work hardening rate *versus* true stress and strain at 1100 °C / 0.01 s⁻¹.

The estimation of the critical stress and strain values marking the DRX initiation showed that with increasing temperature and decreasing strain rate (decreasing Z), the critical stress and strain too decreased. The variation of critical stress and strain for DRX with parameter Z are presented in Fig. 7.

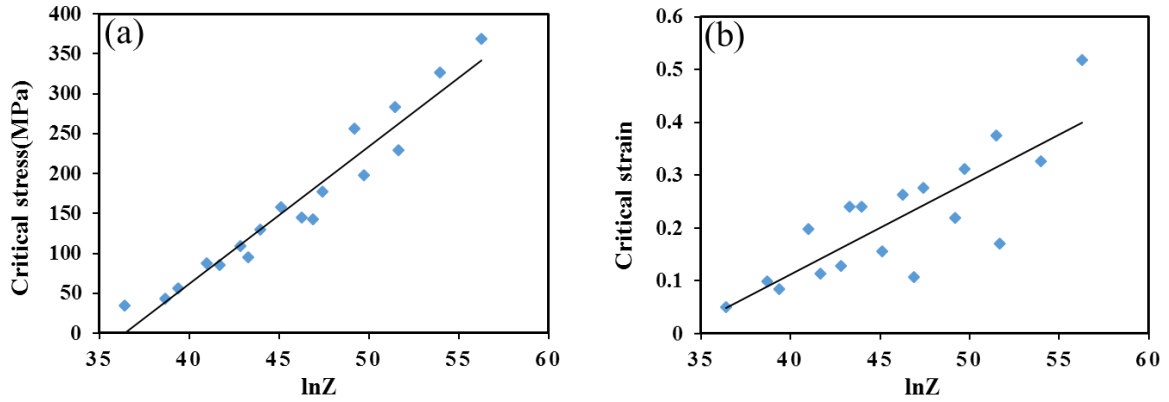


Fig. 7. Critical stress and strain as a function of $\ln Z$

3.3. The hot deformation characteristic parameter model

The typical stress and strain values at peak and critical conditions are related to the Zener-Hollomon parameter by power-law relationships $\sigma = AZ^p$ and $\epsilon = BZ^q$ [15], respectively, where A , B , p and q are constants. The corresponding relationships as a function of the dimensionless parameter Z/A , are shown in Fig. 8.

$$\sigma_P = 0.8901Z^{0.12} = 125.21(Z/A)^{0.12}$$

$$\sigma_C = 0.8278Z^{0.12} = 115.58(Z/A)^{0.12} = 0.93 \sigma_P$$

$$\varepsilon_P = 0.0042Z^{0.0902} = 0.238(Z/A)^{0.0902}$$

$$\varepsilon_C = 0.003Z^{0.0902} = 0.169(Z/A)^{0.0902} = 0.71 \varepsilon_P$$

(6)

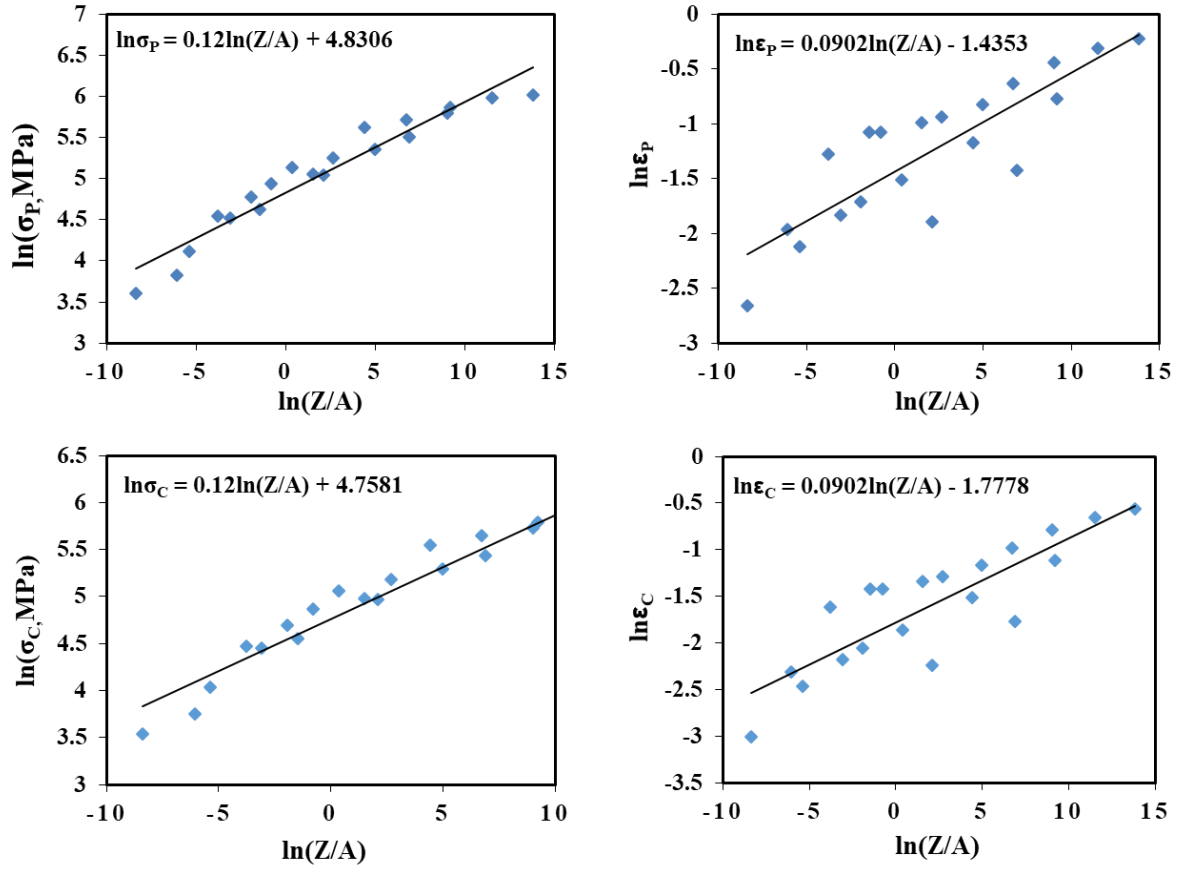


Fig. 8. The characteristic points of the flow curves as a function of Z/A .

3.4. Power dissipation and instability maps

In order to calculate the efficiency of power dissipation (η) and instability parameter (ξ), firstly, the values of flow stress at different temperatures and strain rates were noted at the strain of 0.2, 0.4 and 0.6. Then, the strain rate sensitivity factor (m) was calculated by fitting a third-order polynomial to each logarithmic flow stress-strain rate curve. Accordingly, the first derivative was given the m value. Finally, the values of η and ξ were computed. More details of the computational analysis are described elsewhere [24]. The constructed 2D power dissipation maps showing iso-efficiency contours and corresponding instability maps marking the variation of ξ parameter in temperature-strain rate space plotted for different strains (0.2, 0.4 and 0.6) are exhibited in Figs. 9. Based on the peak efficiency values (Fig 9 a, c and e), the power dissipation maps should be suitably interpreted to determine the safe processing window. It is noteworthy that the parameter η describes the ability of the workpiece to dissipate power through metallurgical processes and should not be misconstrued with the efficiency of the process. As observed, the characteristics of the maps at different strains are similar. In this regard, two deterministic domains can be identified from power dissipation maps and the peak efficiency in these domains varied in a narrow range with strain (Fig. 10):

(I) The first domain is a small domain occurring at 900 °C/0.01 s⁻¹ extending over narrow temperature and strain rate ranges of 820-1000 °C and 0.01-0.05 s⁻¹, with η varying in the range 55-65%.

(II) The other domain is located at relatively high temperatures and intermediate strain rates with peak at about 1200 °C/0.3 s⁻¹, extending over the temperature and strain rate ranges of 1100-1200 °C and 0.1-1 s⁻¹, respectively, with η varying in the range 45-55%.

According to the nature of the flow stress curves (Fig. 5), the governing mechanism for the microstructure formation at these domains is apparently DRX, though the two domains are interestingly far apart and intriguing. According to the instability criterion (Fig 9 b, d and f), a

negative value of ξ represents the instability regime marking unstable flow under the conditions of hot deformation and must be avoided during processing of the material. As can be seen from the instability maps at 0.4 and 0.6 strains (Fig. 9 d and f), the regime of instability (blue and dark green regions corresponding to $\xi = -ve$ up to 0) extend over nearly half of the temperature-strain rate space and delineates the region, where instabilities are likely to manifest during deformation. The instability map of 0.2 strain (Fig. 9 b) was not considered, as the domains/instability regimes at low strains are still developing and cannot be very accurate. As each deterministic domain in the processing map is aptly characterizing the occurrence of a possible microstructural mechanism, a complementary microstructural characterization is inevitably essential to identify the safe/unsafe hot working parameters. Likewise, the instability regime should be suitably characterized with metallographic features to confirm the possible occurrence of unstable flow through manifestation of instabilities that can vary depending on the processing parameters.

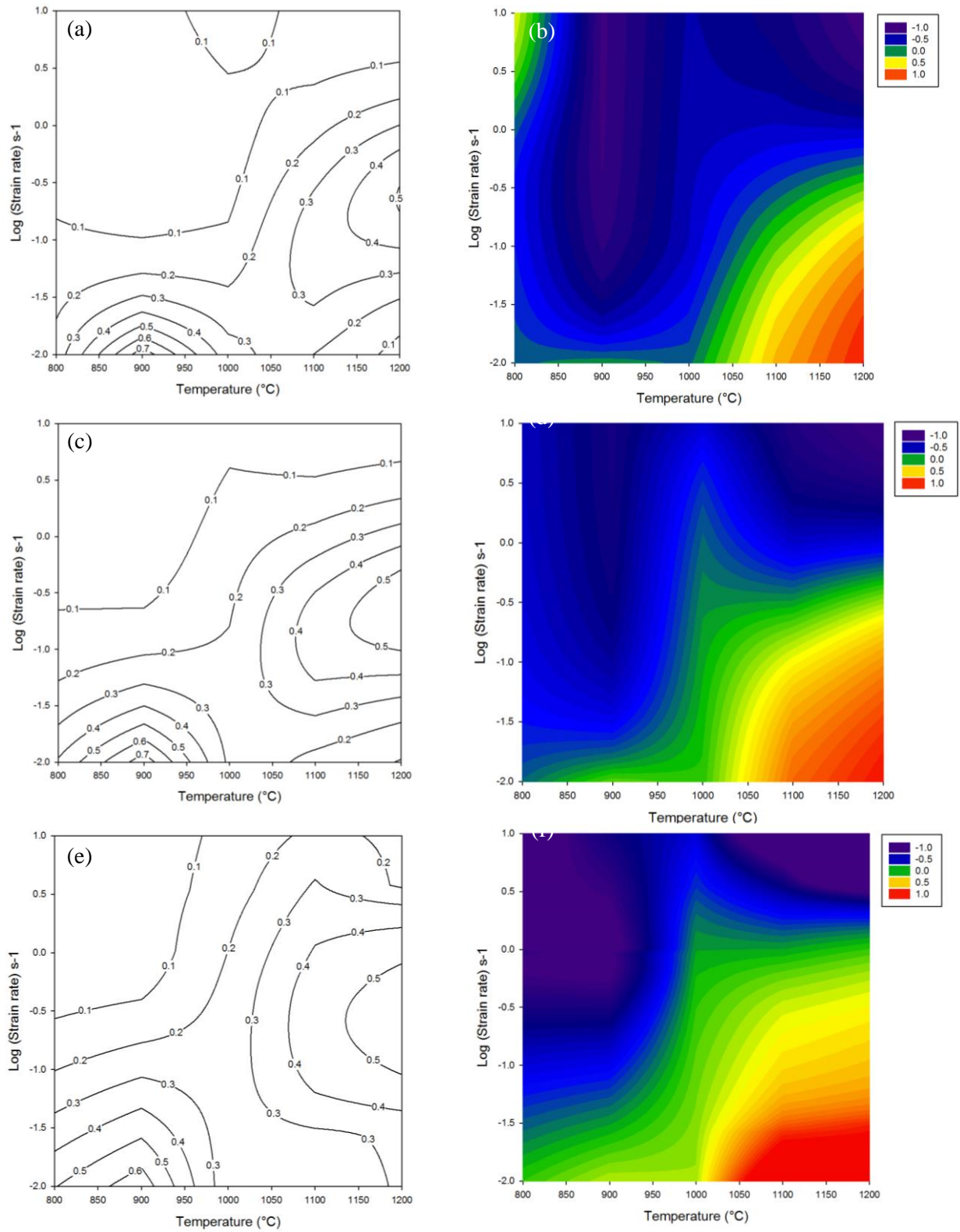


Fig. 9. (a,c,e) The power dissipation maps showing the iso-efficiency contours at the strains of 0.2, 0.4 and 0.6, respectively and (b,d,f) the corresponding instability map showing variation of ξ parameter in temperature-strain rate space at the strain of 0.2, 0.4 and 0.6 respectively.

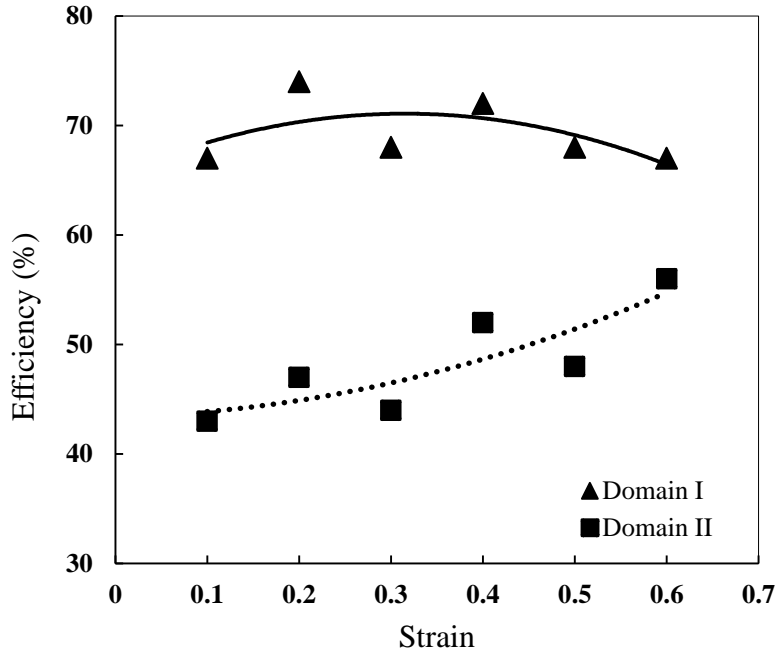


Fig. 10. Variation of peak efficiency of power dissipation with strain for the two deterministic domains identified in the processing map. (i) Domain I represents the lower temperature domain at $900^{\circ}\text{C}/0.01\text{ s}^{-1}$, and (ii) Domain II corresponds to the higher temperature domain with peak at about $1200^{\circ}\text{C}/0.3\text{ s}^{-1}$.

3.5. Microstructural investigation

As discussed, the power dissipation maps need to be interpreted in terms of efficiency of power dissipation and shape of the domains and validated in terms of microstructural processes occurring in different domains. Thus, the two domains obtained in the power dissipation maps for a Ni-free, N-bearing ASS were investigated for microstructural features, as discussed below.

3.5.1. Domain at 900°C and 0.01 s^{-1}

The microstructures of the deformed steel specimens at different hot deformation conditions are shown in Fig. 11. It can be seen that the austenite grains were elongated in the direction of deformation (marked by arrows) and a necklace structure comprising a large number of fine DRX grains decorating the deformed grains formed suggesting the dynamic restoration mechanism occurring in this domain, in accord with the mechanism proposed by Kumar et al

[27] for high nitrogen steels. Due to the high dislocation density, a partial DRX has taken place in the shear bands that manifested during the low temperature deformation, as the instability regime is almost bordering this narrow domain. Increasing the strain rate at 800 °C resulted in a lower DRX fraction, i.e., a tiny necklace structure on initial austenite boundaries at the strain rate of 1 s⁻¹, as the shear banding dominated close to the instability regime (Fig. 11 c). The deformed microstructure at 900 °C/0.01 s⁻¹ (Fig. 11 d) is similar to the condition of 800 °C/0.01 s⁻¹ (Fig. 11 a) showing a necklace structure created by bulging mechanism, in which a higher DRX fraction is achieved at 900 °C. It is to be noted that the dark regions in the microstructure show deformed delta ferrite, which etch strongly and can align along the prior austenite boundaries. The high efficiency of power dissipation in this domain varies in a narrow range (55-65%) with strain, suggesting that it is not a cracking domain, but the high efficiency of power dissipation could be due to the presence of high N content in the steel that can affect its stacking fault energy (SFE) as well [28, 29], which is not ascertained here and is beyond the scope of this study.

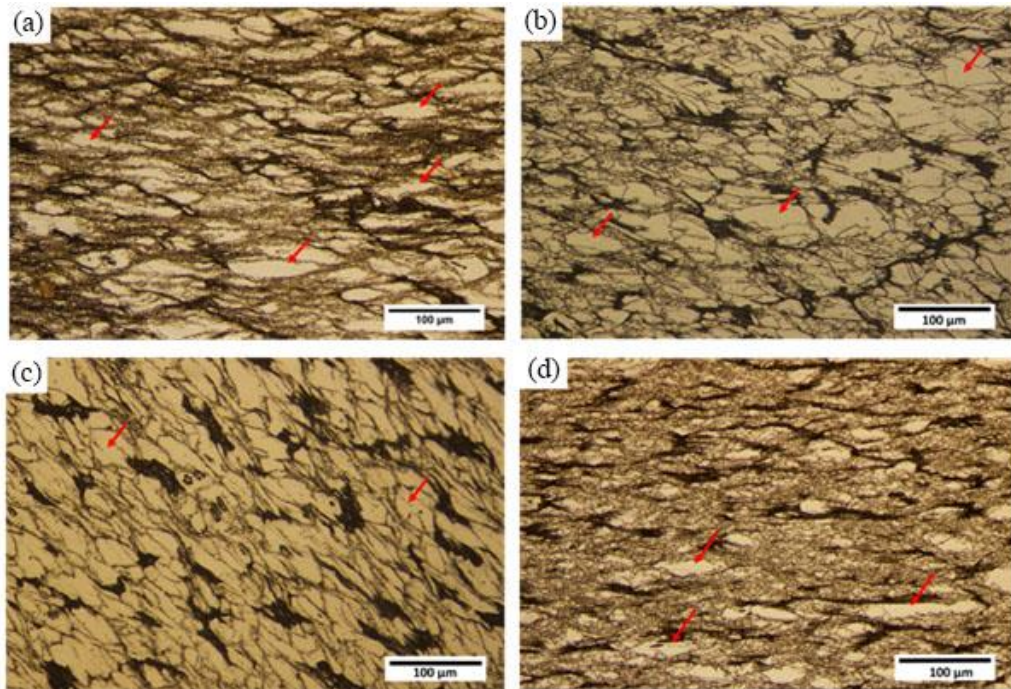


Fig. 11. The microstructure of the steel after hot deformation at (a) 800 °C/0.01 s⁻¹, (b) 800 °C /0.1 s⁻¹, (c) 800 °C/1 s⁻¹, and (d) 900°C/0.01 s⁻¹.

The inverse pole figure (IPF) and grain boundary maps of the steel deformed at 800 °C/0.01 s⁻¹ (Fig. 12) shows that the DRX did not occur in some of the austenite grains and only very low-angle ($2^\circ < \theta < 5^\circ$; green lines) and low-angles boundaries ($5^\circ < \theta < 15^\circ$; red lines) formed. Fig. 12 c shows the magnified IPF map of the necklace region showing a fine grain size structure below 1 μm. Considering the ASS as a low SFE alloy, DRX should occur at high temperatures and intermediate strain rates. On the other hand, the possible influence of high nitrogen in the ASS in slightly increasing the SFE [28, 29] does not completely explain the occurrence of DRX at such low temperatures and strain rates and requires further investigations.

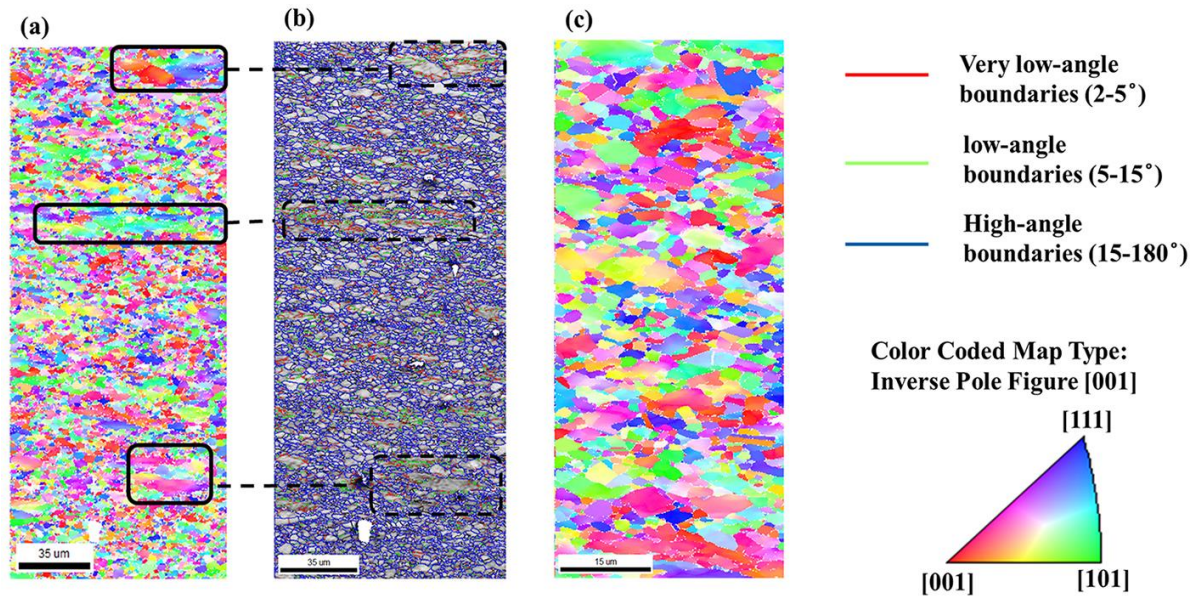


Fig. 12. (a) IPF and (b) grain boundary maps of the ASS deformed at 800 °C/0.01 s⁻¹. The IPF map of the necklace region with higher magnification is shown in (c).

3.5.2. Domain at 1200 °C and 0.3 s⁻¹

The EBSD characterization of the higher temperature domain at 1200 °C/0.3 s⁻¹ combined with LOM showed a completely recrystallized structure in the specimen deformed at 1000 °C/0.01 s⁻¹ consisting of high angle grain boundaries (blue and black lines) (Figs. 13 a-b) that are in good agreement with the LOM image (Fig. 13 c). Only a small fraction of the low-angle and

very low-angle boundaries (green and red lines, respectively) can be observed in the structure. The average grain size of this specimen was about 15 μm , in comparison to the starting grain size of 55 μm . Increasing the strain rate from 0.01 to 10 s^{-1} at temperature of 1000 $^{\circ}\text{C}$ reduced the DRX fraction and caused an incomplete recrystallization at 1 s^{-1} with a mixed microstructure comprising both the deformed grains as well as necklace DRX structure decorating the prior austenite boundaries, as shown in Fig. 14. This location on the map is quite close to the instability regime, see Fig. 9. Microstructural observations in other locations at high temperatures showed that the DRX took place completely in the specimens deformed at 1100 and 1200 $^{\circ}\text{C}$ at all strain rates (Figs. 15 and 16). The presence of significant low-angle (green) and very low-angle (red) boundaries as substructures in the microstructures of these samples confirm the occurrence of DRX. Increasing strain rate from 0.01 to 10 s^{-1} caused a reduction in the DRX grain size due to the lower grain growth (Fig. 15). A higher content of delta ferrite (dark phase in Fig. 16) was also found in the microstructure of samples deformed at 1200 $^{\circ}\text{C}$ compared to that at 1100 $^{\circ}\text{C}$ because of the higher stability at 1200 $^{\circ}\text{C}$, in accord with the equilibrium phase fraction as a function of temperature shown in Fig. 2. The efficiency of power dissipation (45-55 %) in this domain varied in a narrow range (slightly increasing with strain) confirming the occurrence of DRX in this domain and is somewhat higher than reported for the high temperature domains seen in the processing maps of other austenitic stainless steels in literature [30-32]. As stated earlier, the higher efficiency of power dissipation could be due to high N content in the steel, though the effect of delta ferrite, if any, on causing an indirect effect is not easy to understand.

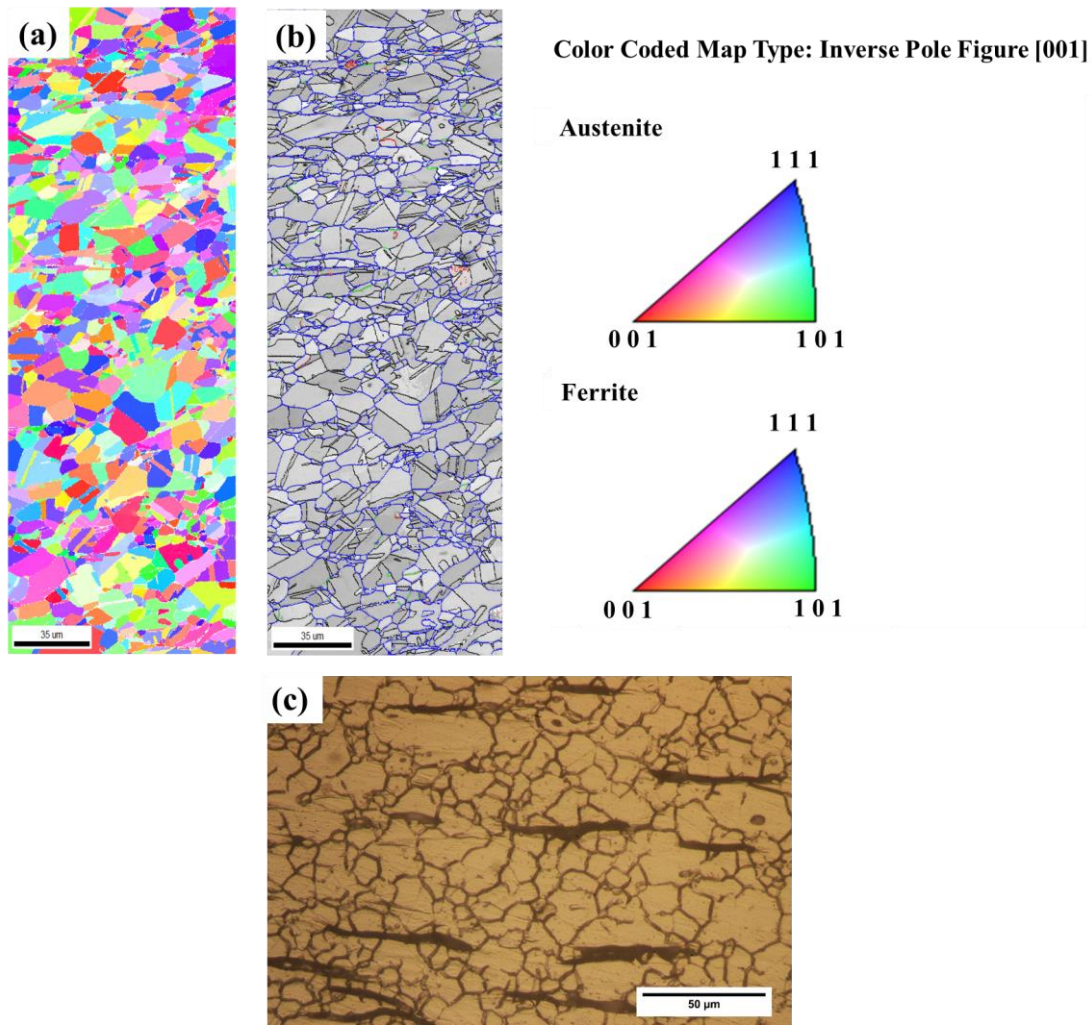


Fig. 13. (a) IPF and (b) grain boundary maps with (c) LOM images of the specimen deformed at $1000\text{ }^{\circ}\text{C}/0.01\text{ s}^{-1}$.

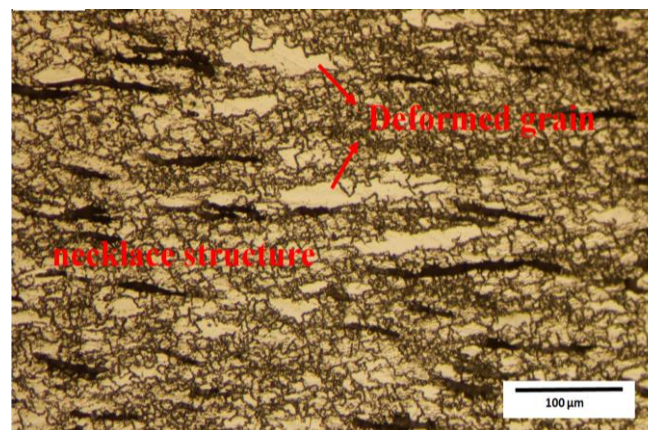


Fig. 14. LOM images of the specimen deformed at $1000\text{ }^{\circ}\text{C}/1\text{ s}^{-1}$.

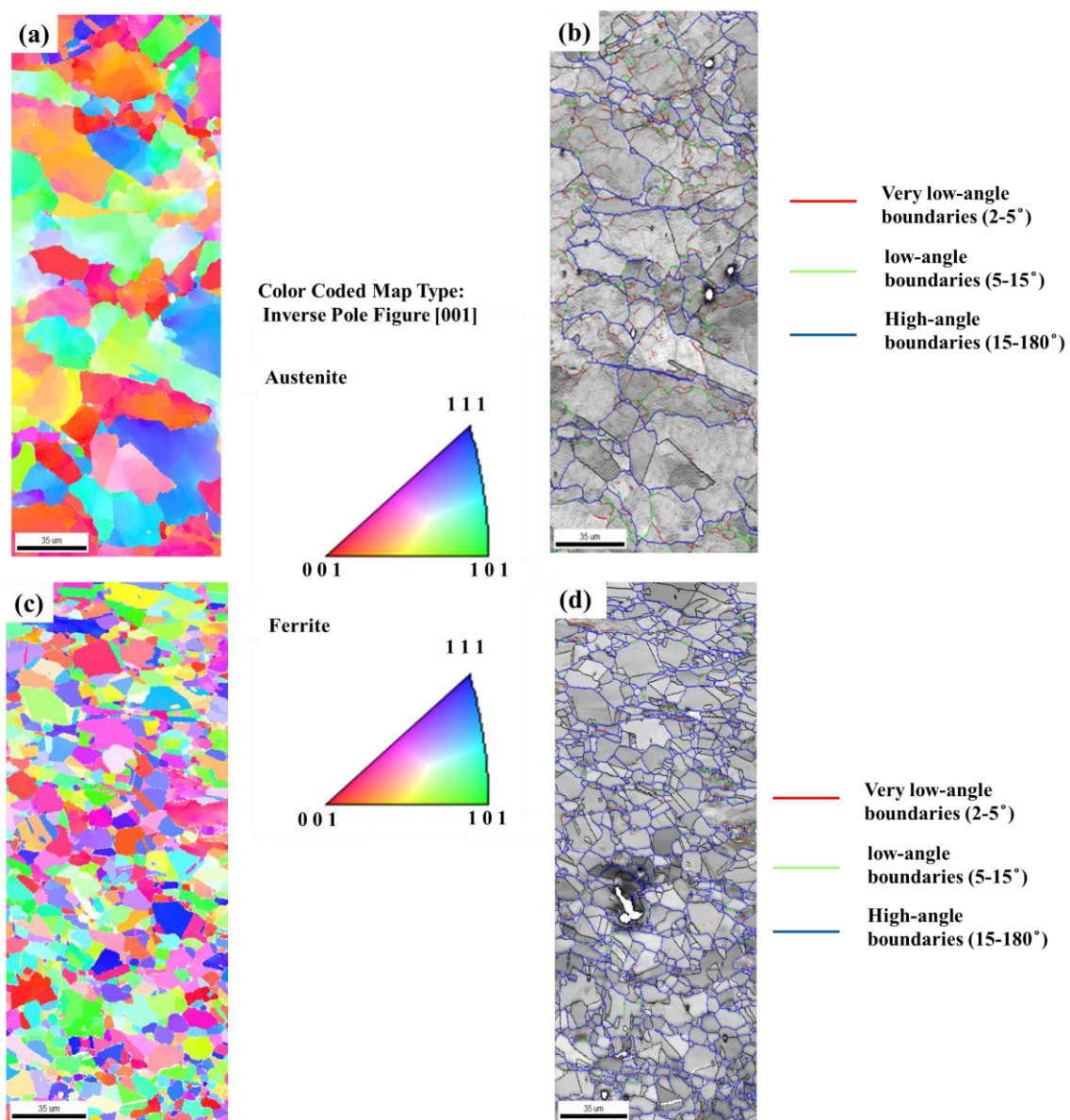


Fig. 15. (a, c) IPF and (b, d) grain boundary maps of the specimen deformed at (a, b) 1100 °C/0.01 s⁻¹ and (c, d) 1100 °C/10 s⁻¹.

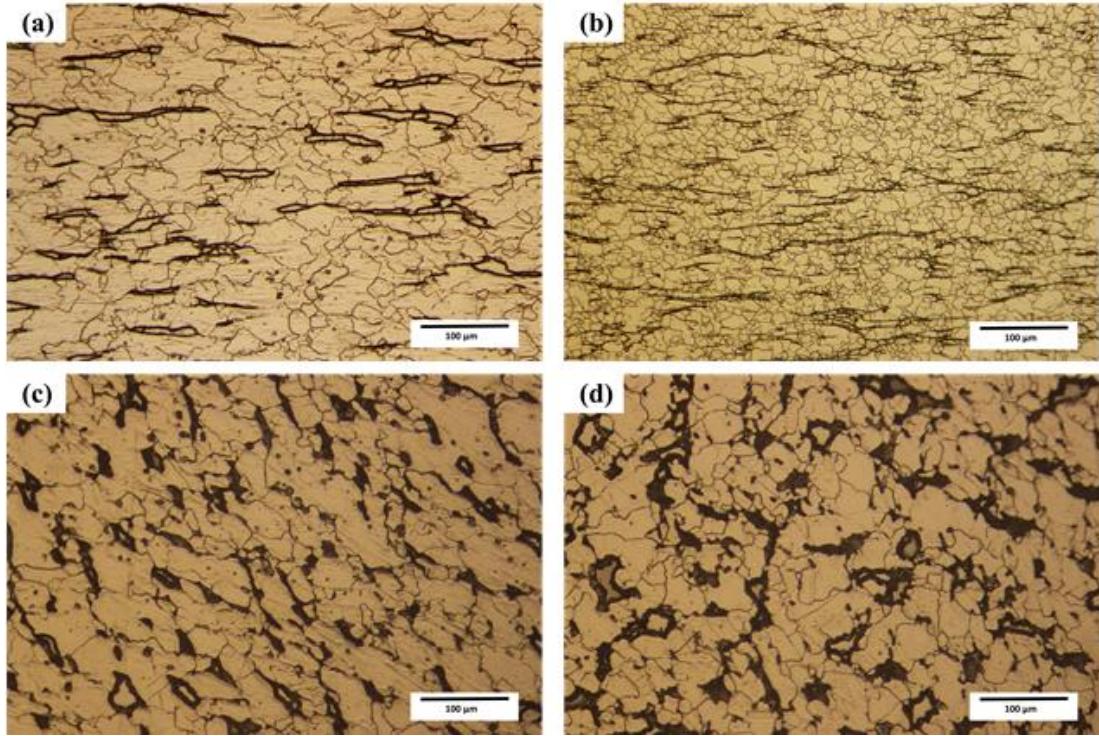


Fig. 16. LOM images of the steels deformed at (a) 1100 °C/0.01 s⁻¹, (b) 1100 °C/10 s⁻¹, (c) 1200 °C/0.01 s⁻¹ and (d) 1200 °C/0.1 s⁻¹.

The pole figures (PF) images of the deformed specimens show that the orientation distribution has changed with increasing temperature at the strain rate of 0.01 s⁻¹ (Fig. 17). The intensity decreased with increasing temperature up to 1000 °C and then increased at 1100 °C because of the grain growth. Similarly, for the specimen deformed at the temperature of 1100 °C, the intensity of the poles in the PF images decreased with increasing strain rate as the rate of grain growth was lower at the strain rate of 10 s⁻¹, as shown in Fig. 18.

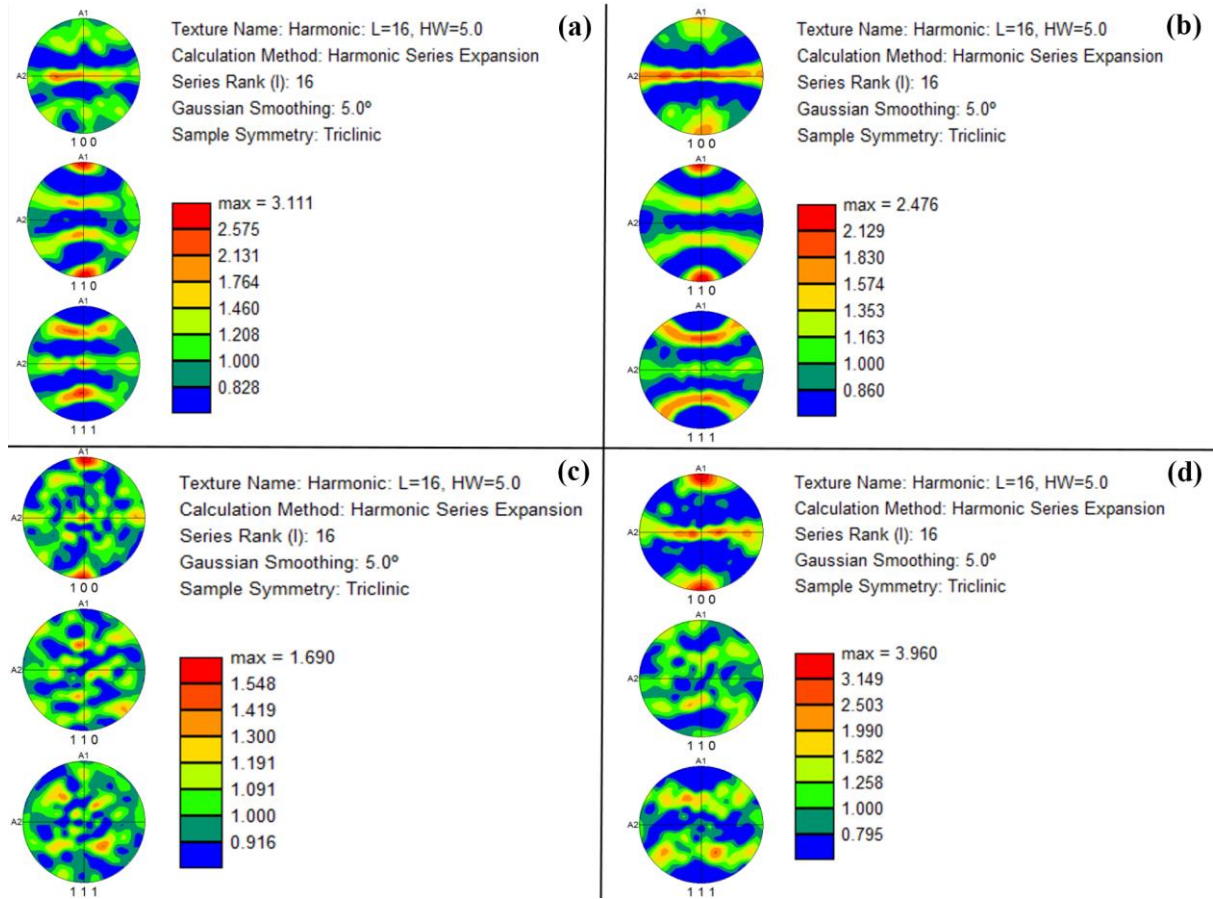


Fig. 17. PF images of specimens deformed under strain rate of 0.01 s^{-1} at temperature of (a) 800 °C, (b) 900 °C, (c) 1000 °C, and (d) 1100 °C.

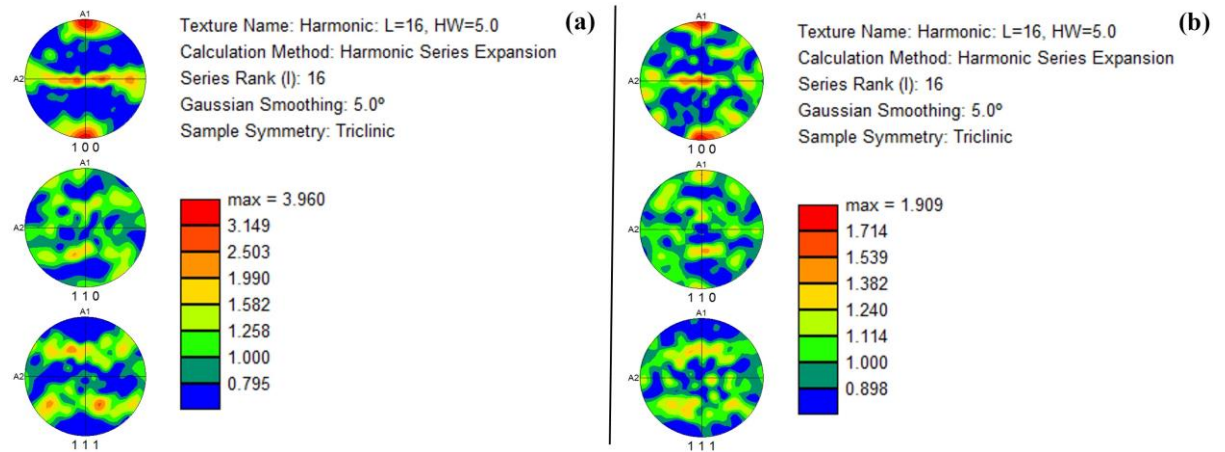


Fig. 18. PF images of specimens deformed at temperature of 1100 °C under strain rate of (a) 0.01 s^{-1} and (b) 10 s^{-1} .

3.5.3. Manifestation of instability

Fig. 19 shows that at 900 °C, the fraction of fine necklace structure decreased, as the strain rate increased from 0.01 to 1 s⁻¹. Consequently, a coarse-grained, deformed austenitic structure was achieved, with substantially reduced recrystallized grains (Fig. 19 c) unlike the necklace structure seen in the case of 900 °C / 0.01 s⁻¹ (Fig. 11 d) sample. This also coincides with the occurrence of instabilities at high strain rates, mainly manifesting as localized shear bands (Fig. 20). At 800 °C and 900 °C / 10 s⁻¹, the region coinciding with relatively high Z conditions, deformation in austenite grains led to pancaked structure besides shear band formation. Therefore, the microstructure in this region is quite complex with operation of a number of mechanisms, mainly pancaking in the grains and localized shear bands and is not desirable for processing.

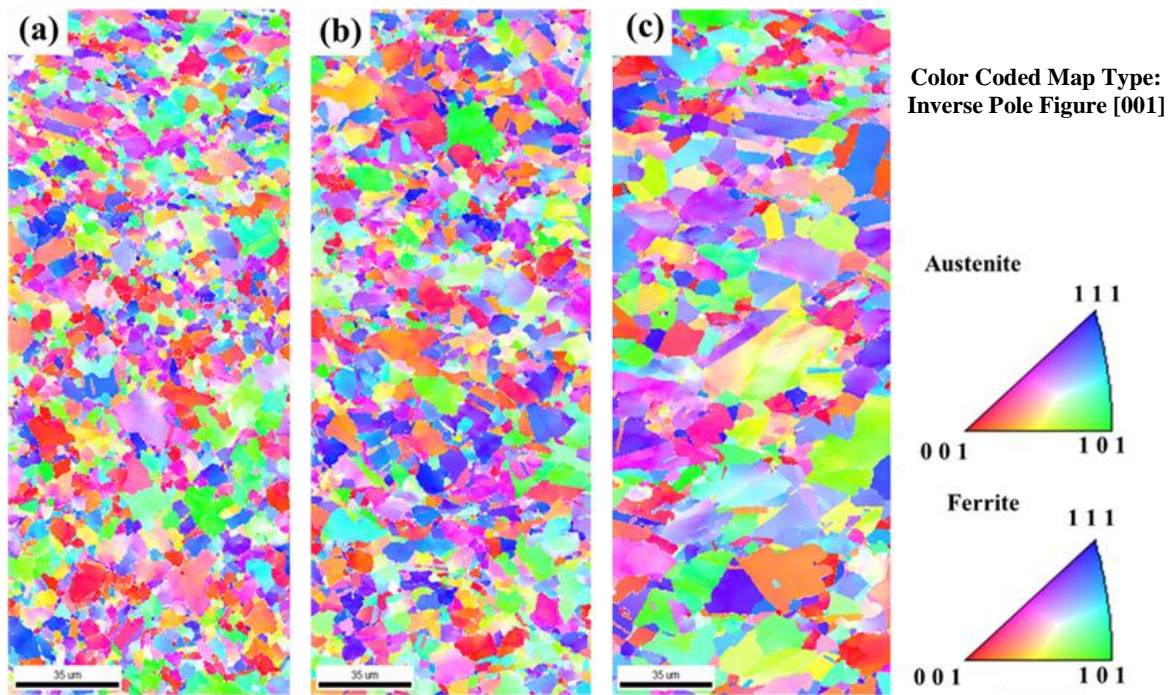


Fig. 19. IPF map of the sample deformed at 900 °C and strain rate of (a) 0.01, (b) 0.1, and (c) 1 s⁻¹.

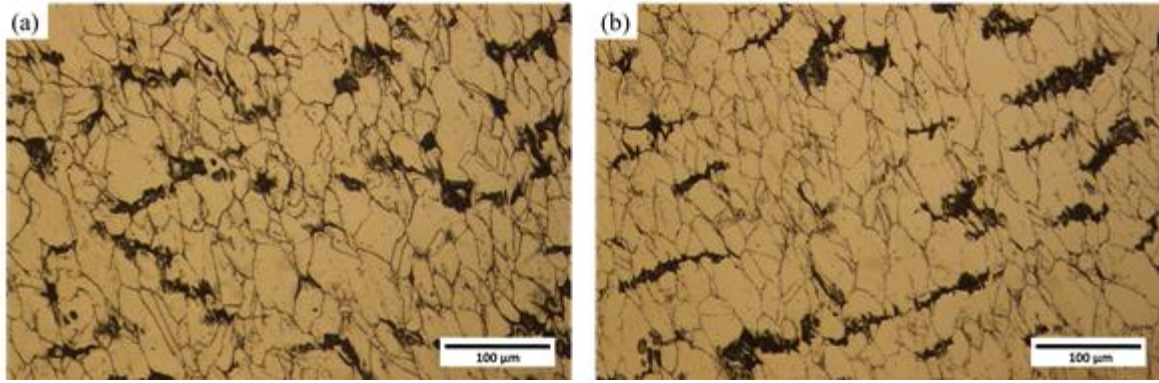


Fig. 20. OM image of the steel after hot deformation at (a) 800 °C/10 s⁻¹ (b) 900 °C/10 s⁻¹.

3.6. Processing map for the Ni-free ASS

By superimposing the instability map on the power dissipation map, validated using the microstructural observations, a conceptual processing map, as shown in Fig. 21, is suggested to describe the hot deformation of the investigated Ni-free ASS containing 0.28 wti. % N in the temperature and strain rate ranges of 800-1200 °C and 0.01 to 10 s⁻¹, respectively. Based on the amount of η , ξ and the corresponding microstructures, the most reliable regime for the DRX is located at the temperature range of 1100-1200 °C and the strain rate of 0.01-1 s⁻¹ in which a positive value obtained for the instability parameter and the efficiency of power dissipation stays $\geq 40\%$. For practical applications, it is possible to achieve a fully refined DRX microstructure by high-speed deformation (> 1 s⁻¹) at temperatures above 1100 °C without any microstructural flaws, but the instability regime must be avoided to prevent manifestation of the defects in the microstructures.

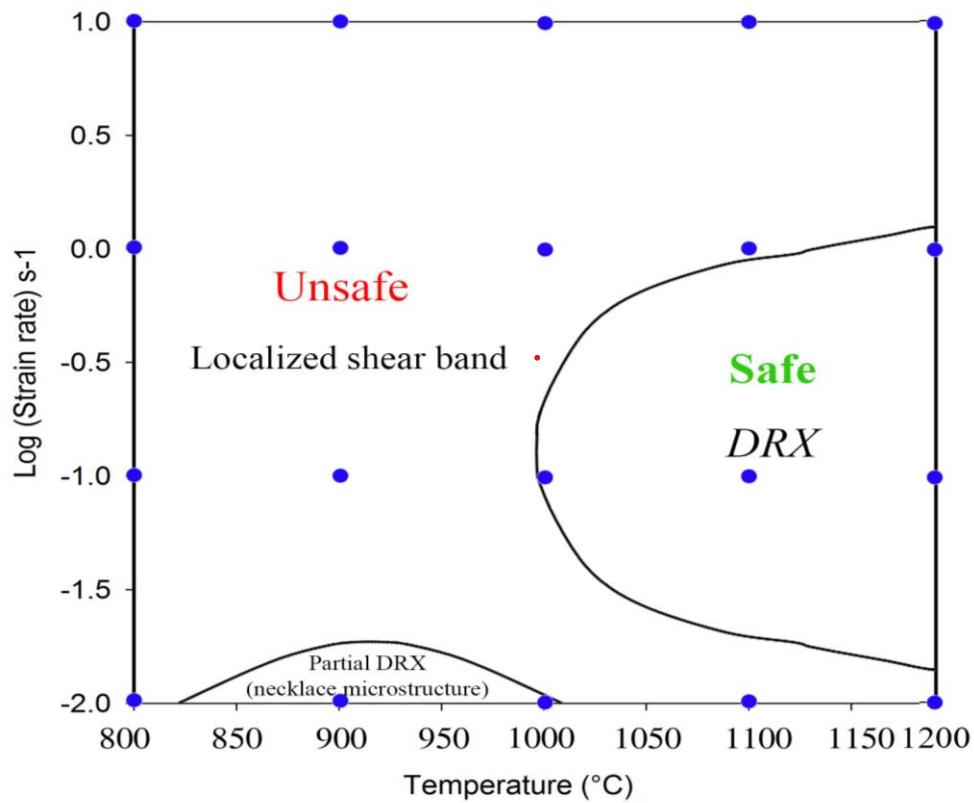


Fig. 21. Processing map for the investigated Ni-free ASS containing 0.28 wt.% N .

4. Conclusions

In this study, the hot deformation processing map of a Ni-free ASS containing 0.28 wt. % N was developed. The main conclusions can be drawn as follows:

- 1) The critical stress and strain for DRX occurrence decreased with increasing deformation temperature and decreasing strain rate.
- 2) Deformation at low temperatures (800 to 1000 °C) led to the formation of a necklace microstructure with the deformed and recrystallized grains.
- 3) A fully DRX structure was achieved at the temperature range of 1000-1200 °C and the strain rate of $0.01-1 \text{ s}^{-1}$. By increasing deformation temperature, higher strain rate could be applied, safely.
- 4) The optimum condition of hot deformation to achieve a fine recrystallized microstructure without any deformation defects was located at the condition of 1000 °C/ 0.01 s^{-1} .

5) The processing map reveals that it is possible to achieve a fully refined DRX microstructure by high-speed deformation ($> 1 \text{ s}^{-1}$) at temperatures above $1100 \text{ }^{\circ}\text{C}$ without any microstructural flaws.

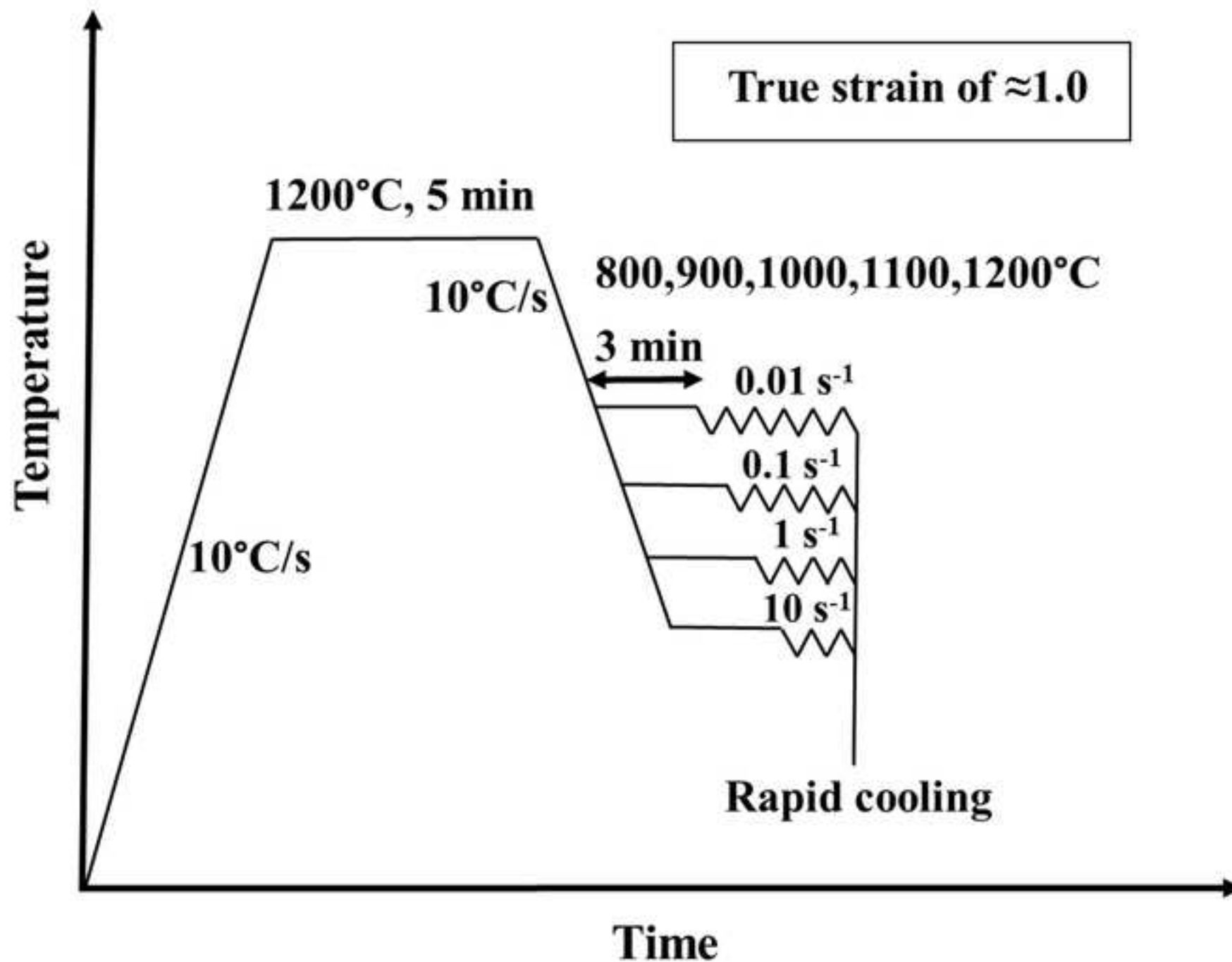
References

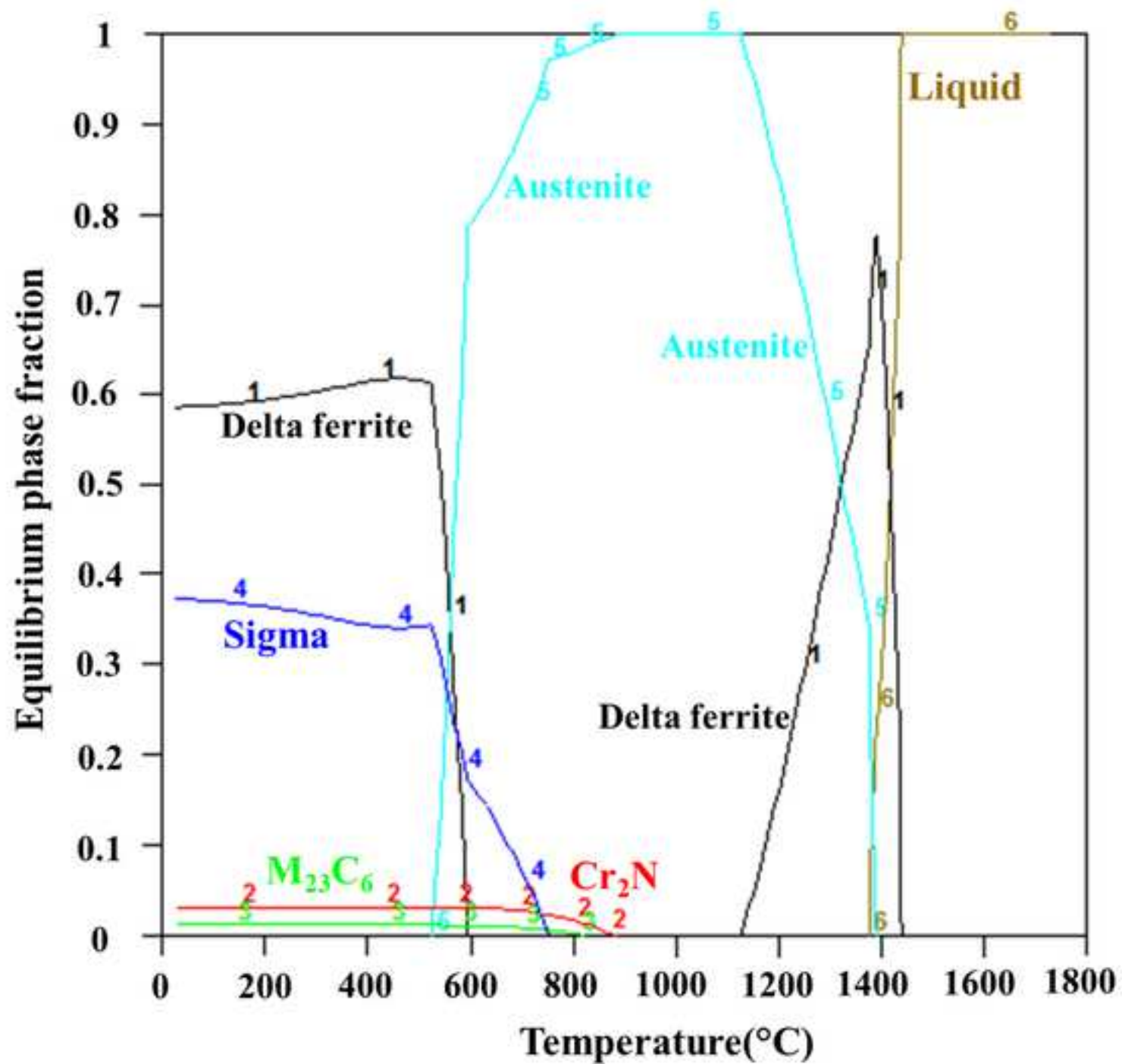
- [1] K.H. Lo, C.H. Shek and J.K.L. Lai, "Recent developments in stainless steels", *Mater. Sci. Eng. R*, 65 (2009) pp. 39–104. <https://doi.org/10.1016/j.mser.2009.03.001>.
- [2] J.W. Simmons, "Overview: high-nitrogen alloying of stainless steels", *Mater. Sci. Eng. A*, 207 (1996) pp. 159–169. [https://doi.org/10.1016/0921-5093\(95\)09991-3](https://doi.org/10.1016/0921-5093(95)09991-3).
- [3] G. Balachandran, M. L. Bhatia, N. B. Ballal and P. Krishna, "Some theoretical aspects on designing nickel free high nitrogen austenitic stainless steels", *ISIJ Int.*, 41 (2001) pp. 1018–1027. <https://doi.org/10.2355/isijinternational.41.1018>.
- [4] D.W. Kim, "Influence of nitrogen-induced grain refinement on mechanical properties of nitrogen alloyed type 316LN stainless steel", *J. Nucl. Mater.*, 420 (2012) pp. 473–478. <https://doi.org/10.1155/2015/427945>.
- [5] Z. Jiang, Z. Zhang, H. Li, Z. Li, and Q. Ma, "Microstructural evolution and mechanical properties of aging high nitrogen austenitic stainless steels", *Int. J. Min., Metall. Mater.*, 17 (2010) pp. 729–736. <https://doi.org/10.1007/s12613-010-0381-x>.
- [6] M. Saucedo-Muñoz, Y. Watanabe, T. Shoji, and H. Takahashi, "Effect of microstructure evolution on fracture toughness in isothermally aged austenitic stainless steels for cryogenic applications" *Cryogen.*, 40 (2000) pp. 693–700. [https://doi.org/10.1016/S0011-2275\(01\)00004-2](https://doi.org/10.1016/S0011-2275(01)00004-2).
- [7] H. Ha, T. Lee, C. Oh, and S. Kim, "Effects of combined addition of carbon and nitrogen on pitting corrosion behavior of Fe-18Cr-10Mn alloys", *Scrip. Mater.*, 61 (2009) pp. 121–124. <https://doi.org/10.1016/j.scriptamat.2009.03.018>.
- [8] T. Sakai, A. Belyakov, R. Kaibyshev, H. Miura, and J.J. Jonas, "Dynamic and post-dynamic recrystallization under hot, cold and severe plastic deformation conditions", *Prog. Mater. Sci.*, 60 (2014) pp. 130–207. <https://doi.org/10.1016/j.pmatsci.2013.09.002>.

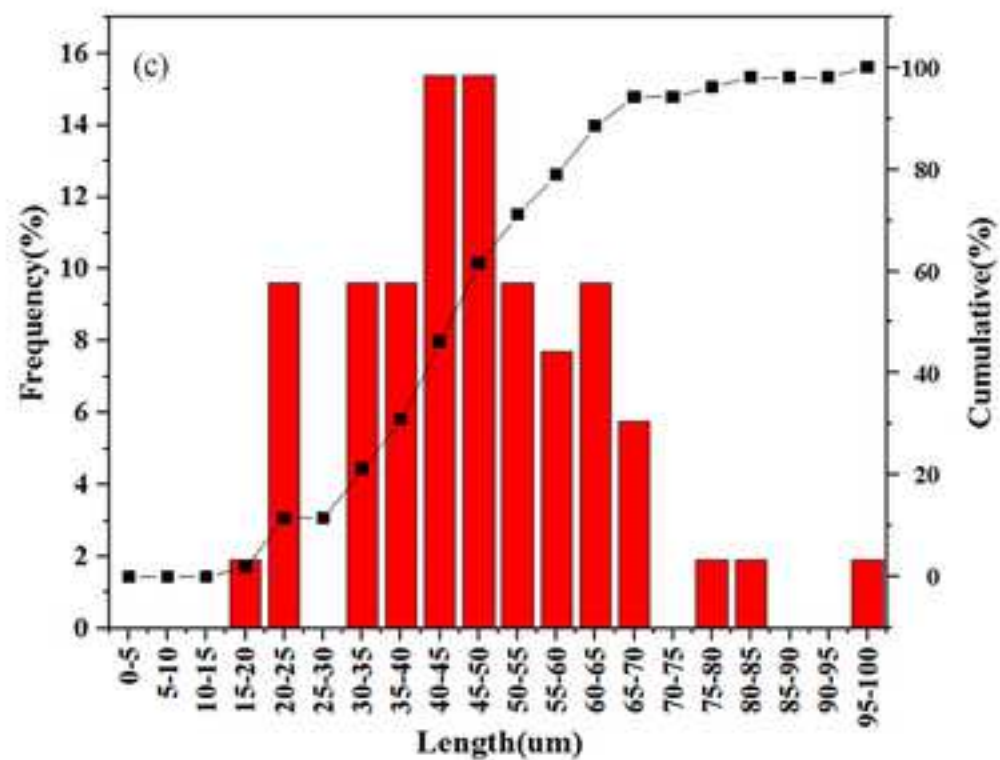
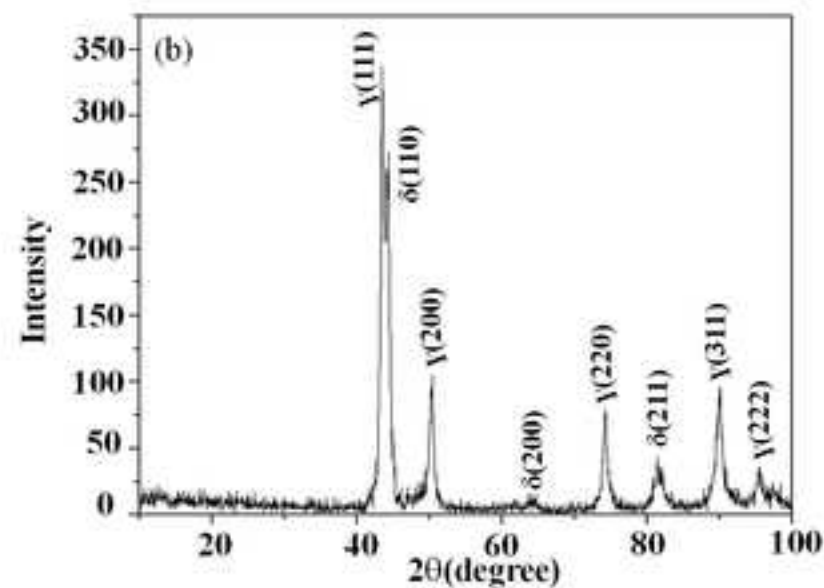
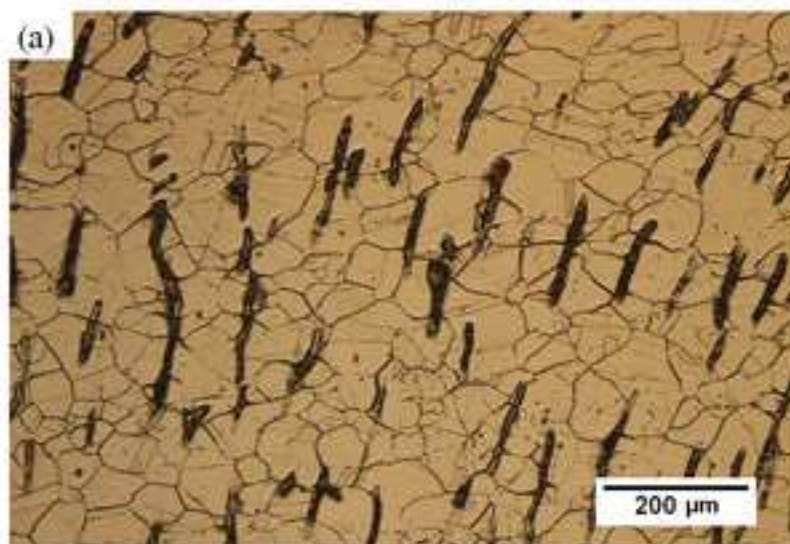
- [9] M. E. Wahabi, J.M. Cabrera, J.M. Prado, "Hot working of two AISI 304 steels: a comparative study", *Mater. Sci. Eng. A*, 343 (2003) pp. 116-125. [https://doi.org/10.1016/S0921-5093\(02\)00357-X](https://doi.org/10.1016/S0921-5093(02)00357-X).
- [10] A. Dehghan-Manshadi, M.R. Barnett and P.D. Hodgson, "Hot deformation and recrystallization of austenitic stainless steel: Part I. dynamic recrystallization", *Metall. Mater. Trans. A*, 39 (2008) pp. 1359–1370. <https://dx.doi.org/10.1007/s11661-008-9513-6>.
- [11] S.K. Rajput, G.P. Chaudhari, S.K. Nath, "Characterization of hot deformation behavior of a low carbon steel using processing maps, constitutive equations and Zener Hollomon parameter", *J. Mater. Proc. Technol.*, 237 (2016) pp. 113-125. <https://doi.org/10.1016/j.jmatprotec.2016.06.008>.
- [12] M. Rout, R. Ranjan, S. K. Pal, Sh. B. Singh, "EBSD study of microstructure evolution during axisymmetric hot compression of 304LN stainless steel", *Mater. Sci. Eng. A*, 711 (2018) pp. 378–388. <https://doi.org/10.1016/j.msea.2017.11.059>.
- [13] Y. Zhou, Y. Liu, X. Zhou, C. Liu, J. Yu, Y. Huang, H. Li, W. Li, "Precipitation and hot deformation behavior of austenitic heat-resistant steels" A review, *Mater. Sci. Technol.*, 33 (2017) pp. 1448-1456. <https://doi.org/10.1016/j.jmst.2017.01.025>.
- [14] L. Xu, L. Chen, G. Chen , M. Wang, "Hot deformation behavior and microstructure analysis of 25Cr3Mo3NiNb steel during hot compression tests", *Vacuum*, 147 (2018) pp. 8-17. <https://doi.org/10.1016/j.vacuum.2017.10.017>.
- [15] H. Mirzadeh, J. Cabrera, and A. Najafizadeh, "Modeling and prediction of hot deformation flow curves", *Metall. Mater. Trans. A*, 43(2012) pp. 108-123. <https://doi.org/10.1007/s11661-011-0836-3>.
- [16] H. Mirzadeh, J. Cabrera, A. Najafizadeh, "Constitutive relationships for hot deformation of austenite", *Acta Mater.*, 59 (2011) pp. 6441-6448. <https://doi.org/10.1016/j.actamat.2011.07.008>.
- [17] H. Mirzadeh, A. Najafizadeh and M. Moazeny, "Flow curve analysis of 17-4 PH stainless steel under hot compression test", *Metall. Mater. Trans. A*, 40 (2009) pp. 2950–2958. <https://dx.doi.org/10.1007/s11661-009-0029-5>.
- [18] R.K.C. Nkhoma, C. W. Siyasiya and W.E. Stumpf, "Hot workability of AISI 321 and AISI 304 austenitic stainless steels", *J. Alloy. Comp.*, 595 (2014) pp. 103–112. <https://doi.org/10.1016/j.jallcom.2014.01.157>.

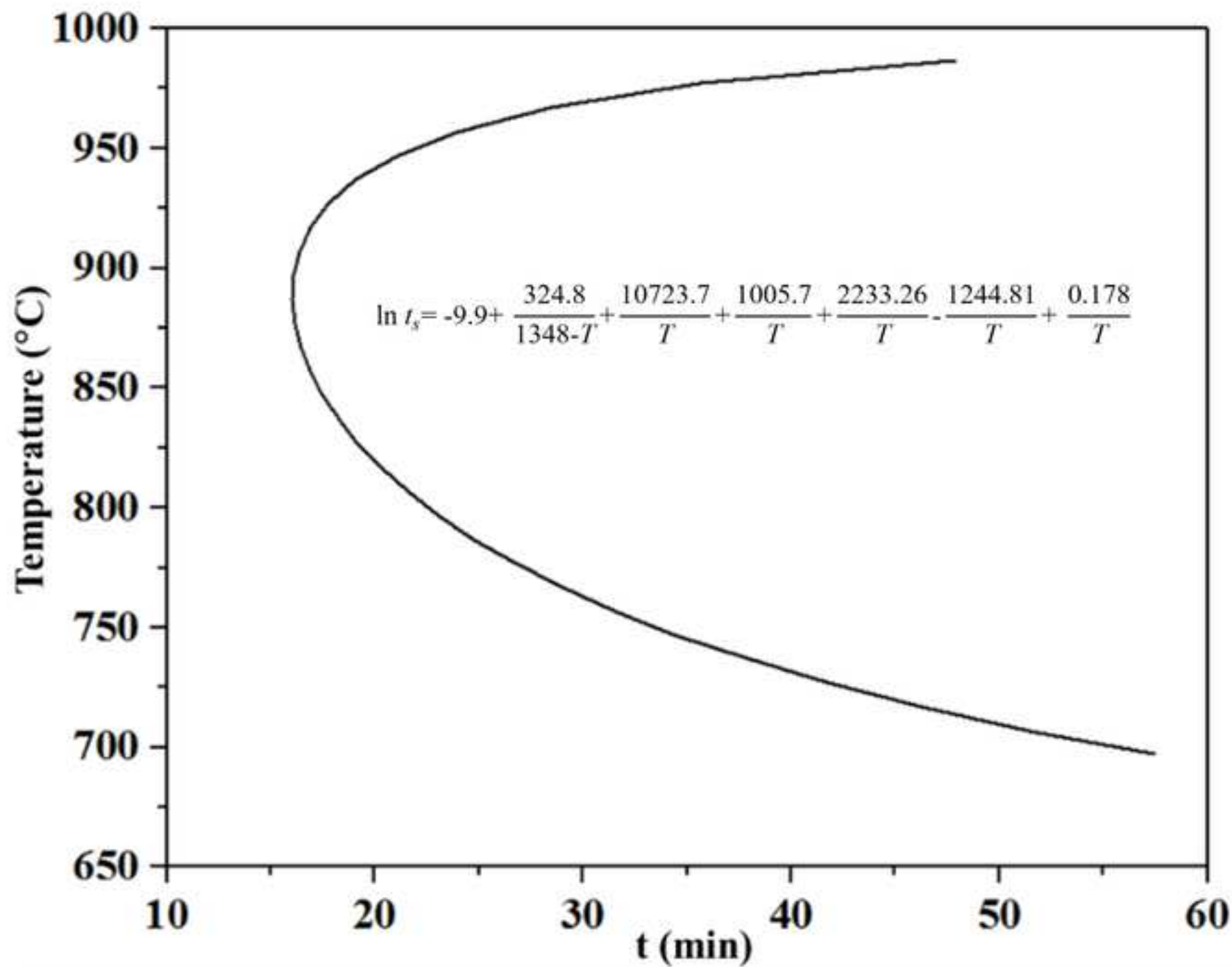
- [19] P. Yang, C. Liu, Q. Guo, Y. Liu, "Variation of activation energy determined by a modified Arrhenius approach: Roles of dynamic recrystallization on the hot deformation of Ni-based superalloy", *Mater. Sci. Technol.*, 72 (2021), pp. 162-171. <https://doi.org/10.1016/j.jmst.2020.09.024>.
- [20] Z. Wang, W. Fu, S. Sun, H. Li, Z. Lv and D. Zhao, "Mechanical Behavior and Microstructural Change of a High Nitrogen CrMn Austenitic Stainless Steel during Hot Deformation", *Metall. Mater. Trans. A*, 41 (2010) pp. 1025–1032. <https://doi.org/10.1007/S11661-009-0153-2>.
- [21] J. Moon, T. Lee, J. Shin and J. Lee, "Hot working behavior of a nitrogen-alloyed Fe-18Mn-18Cr-N austenitic stainless steel", *Mater. Sci. Eng. A*, 594 (2014) pp. 302–308. <https://doi.org/10.1016/j.msea.2013.11.090>.
- [22] T. Xi, C. Yang, M. Babar Shahzad, K. Yang, "Study of the processing map and hot deformation behavior of a Cu-bearing 317LN austenitic stainless steel", *Mater. Des.*, 87 (2015) pp. 303–312. <https://doi.org/10.1016/j.matdes.2015.08.011>.
- [23] H. Rastegari, A. Kermanpur, A. Najafizadeh, M.C. Somani, D.A. Porter, E. Ghassemali, A.E.W. Jarfors, "Determination of processing maps for the warm working of vanadium microalloyed eutectoid steels", *Mater. Sci. Eng. A*, 658 (2016), pp.167-175. <https://doi.org/10.1016/j.msea.2016.01.088>.
- [24] H. Rastegari, A. Kermanpur, A. Najafizadeh, D.A. Porter, M.C. Somani, "Warm deformation processing maps for the plain eutectoid steels", *J. Alloy. Comp.*, 626 (2015) pp.136-144. <https://doi.org/10.1016/j.jallcom.2014.11.170>.
- [25] Q.X. Dai, Z.Z. Yuan, X.M. Luo, X.N. Cheng, "Numerical simulation of Cr₂N age-precipitation in high nitrogen stainless steels", *Mater. Sci. Eng. A*, 385 (2004) pp. 445-448. <https://doi.org/10.1016/j.msea.2004.07.003>.
- [26] H. Khorshidi, A. Kermanpur, M.C. Somani, and A. Najafizadeh, "On the hot deformation behavior of a Ni-free austenitic stainless steel interstitially alloyed with low nitrogen content", *J. Mater. Eng. Perform.*, 27 (2018) pp. 6765–6779. <https://doi.org/10.1007/s11665-018-3766-z>.
- [27] S. Kumar, B. Aashranth, D. Samantaray, M. Arvinth Davinci, U. Borah, A.K. Bhaduri, "Influence of nitrogen on kinetics of dynamic recrystallization in Fe-Cr-Ni-Mo steel", *Vacuum*, 156 (2018) pp. 20-29. <https://doi.org/10.1016/j.vacuum.2018.07.010>.

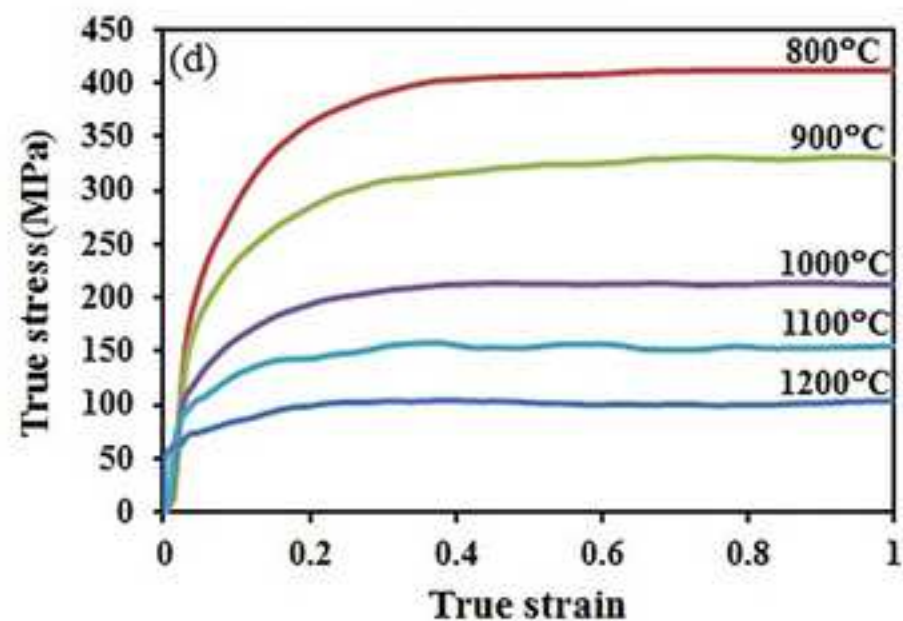
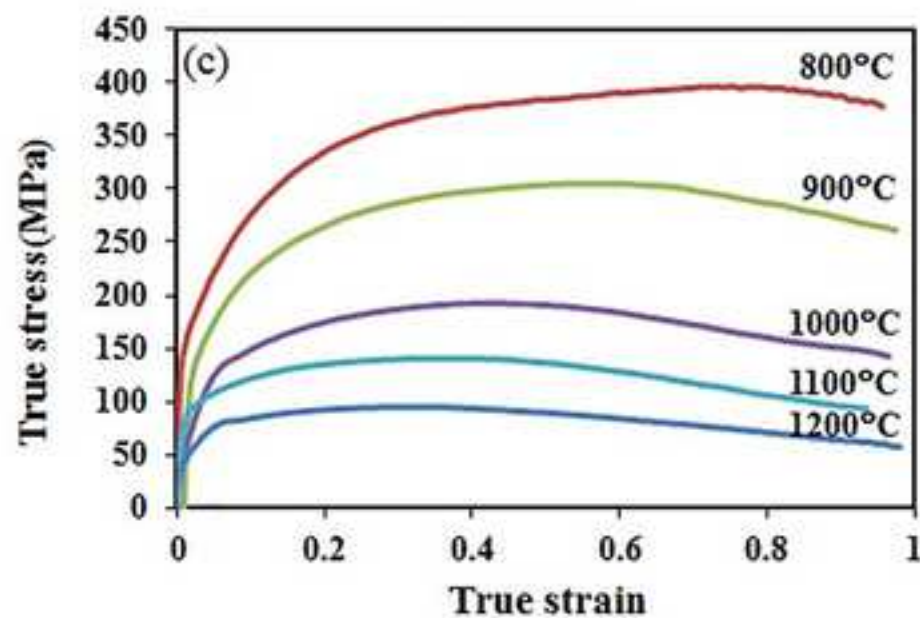
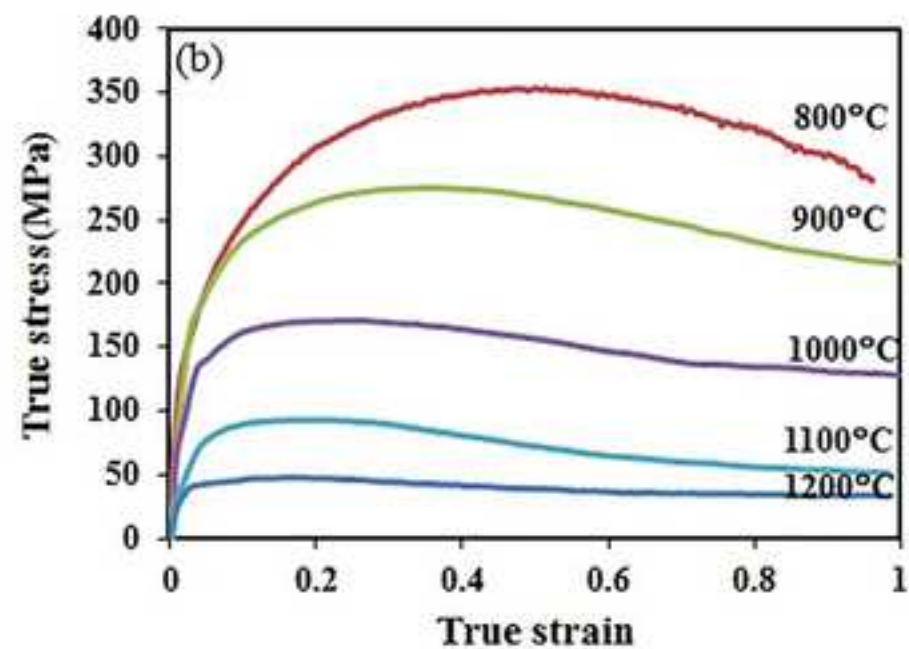
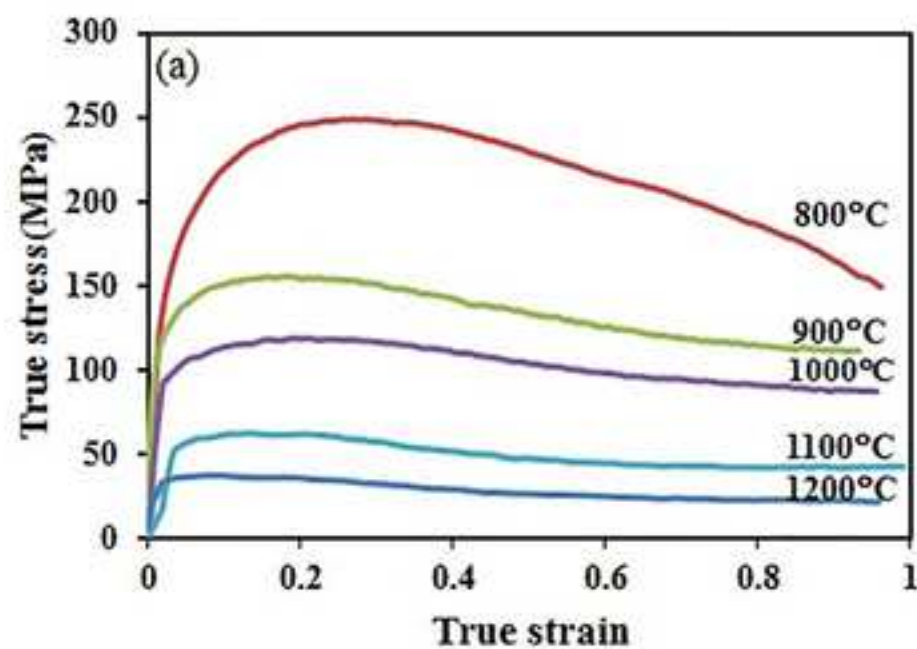
- [28] I. A. Yakubtsov, A. Ariapour and D. D. Perovic, "Effect of Nitrogen on Stacking Fault Energy of F.C.C. Iron-Based Alloys", *Acta Mater.*, 47 (1999) pp. 1271-1279. [https://doi.org/10.1016/S1359-6454\(98\)00419-4](https://doi.org/10.1016/S1359-6454(98)00419-4).
- [29] L. Mosecker and A. Saeed-Akbari, "Nitrogen in chromium-manganese stainless steels: a review on the evaluation of stacking fault energy by computational thermodynamics", *Sci. Technol. Adv. Mater.*, 14 (2013). <https://doi.org/10.1088/1468-6996/14/3/033001>.
- [30] Yinghui Zhou, Yongchang Liu, Xiaosheng Zhou, Chenxi Liu, Liming Yu, and Chong Li, "Processing maps and microstructural evolution of the type 347H austenitic heat-resistant stainless steel", *J. Mater. Res.*, 30 (2015) pp. 2090-2100. <https://doi.org/10.1557/jmr.2015.168>.
- [31] J. Rasti, "Grain Size Effect on the Hot Deformation Processing Map of AISI 304 Austenitic Stainless Steel", *Int. J. ISSI*, 15 (2018) pp. 54-61.
- [32] K. Arun Babu, S. Mandal, C.N. Athreya, B. Shakthipriya, V. Subramanya Sarma, "Hot deformation characteristics and processing map of a phosphorous modified super austenitic stainless steel", *Mater. Des.*, 115 (2016) pp. 262-275. <https://doi/10.1016/j.matdes.2016.11.054>.

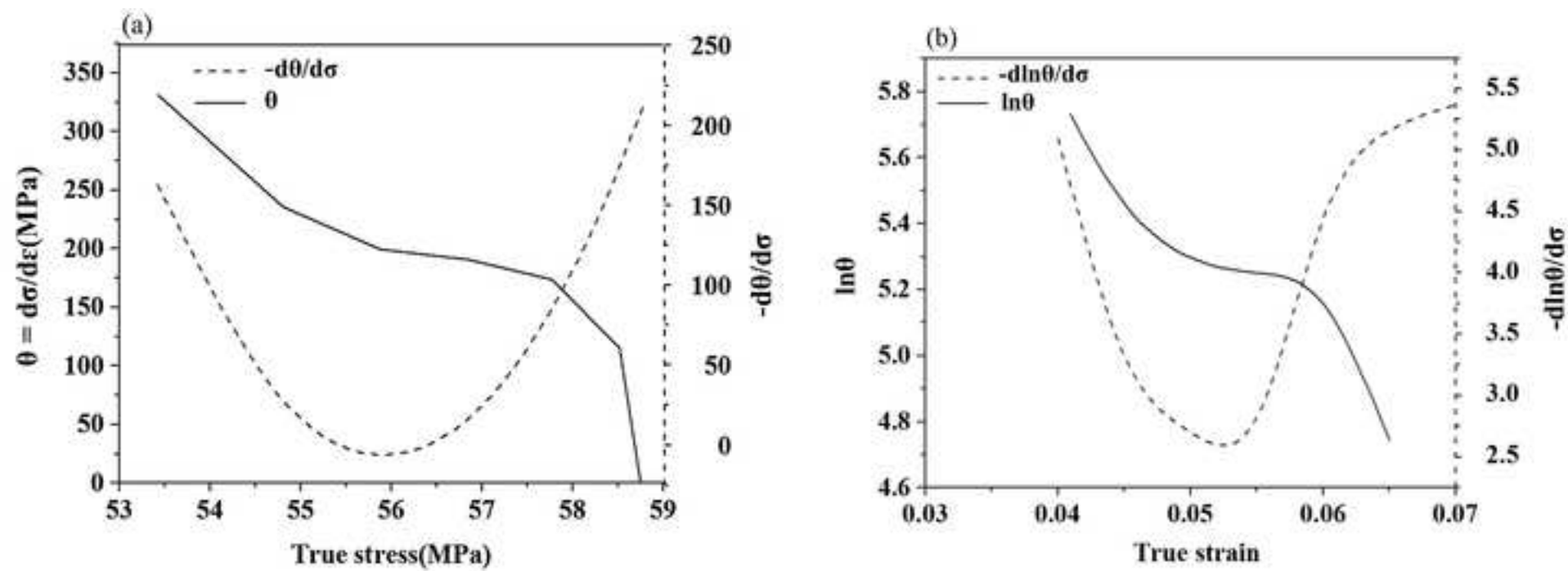


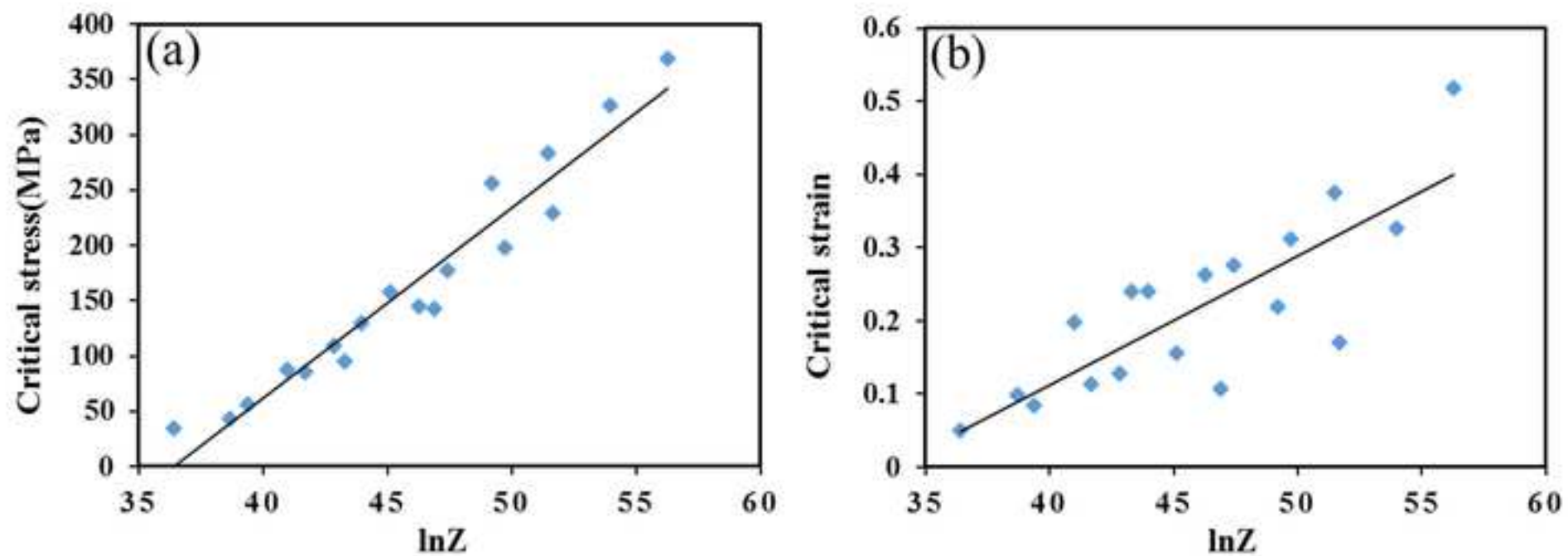


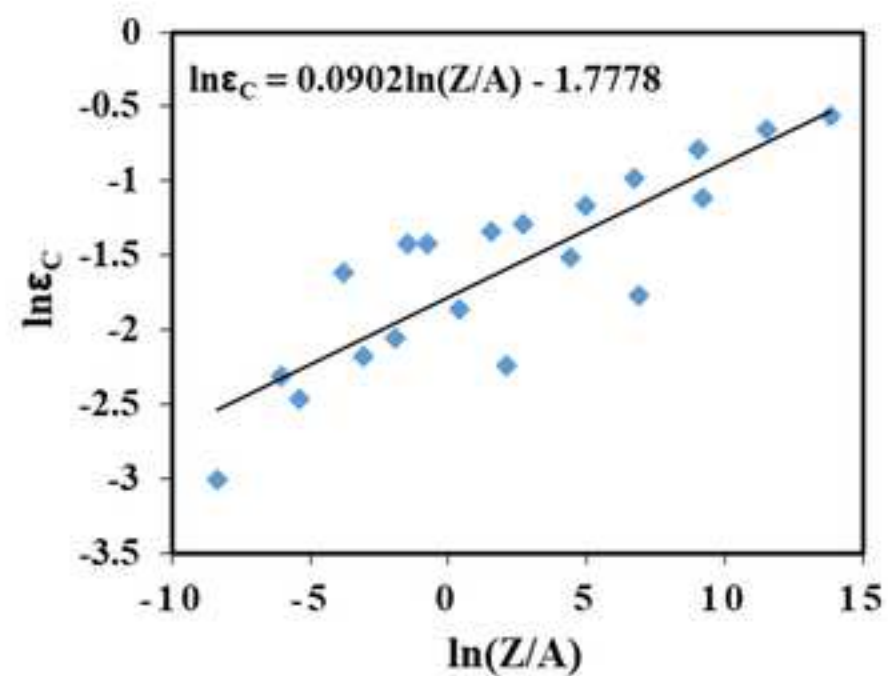
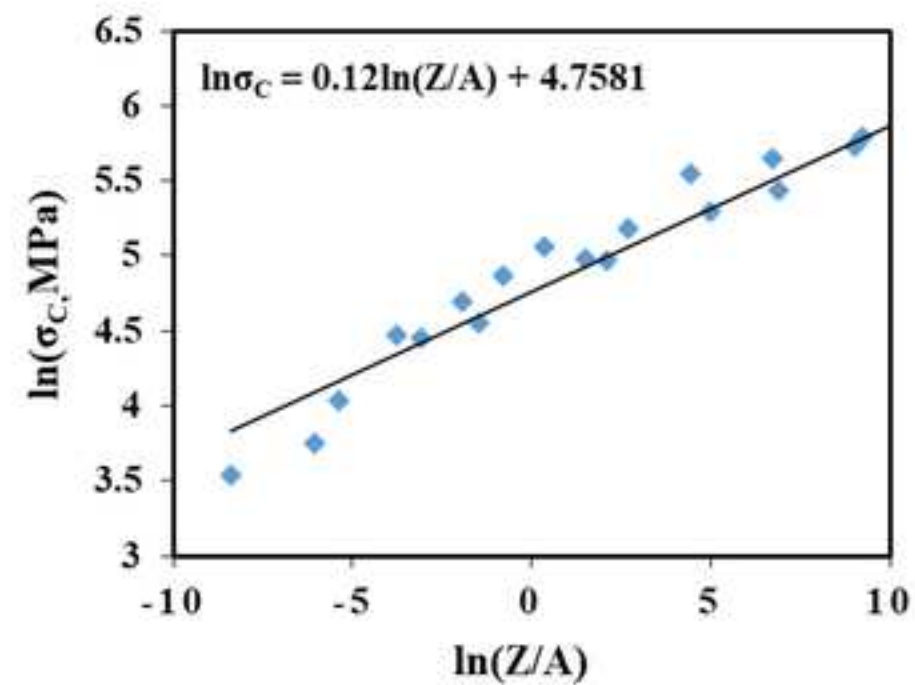
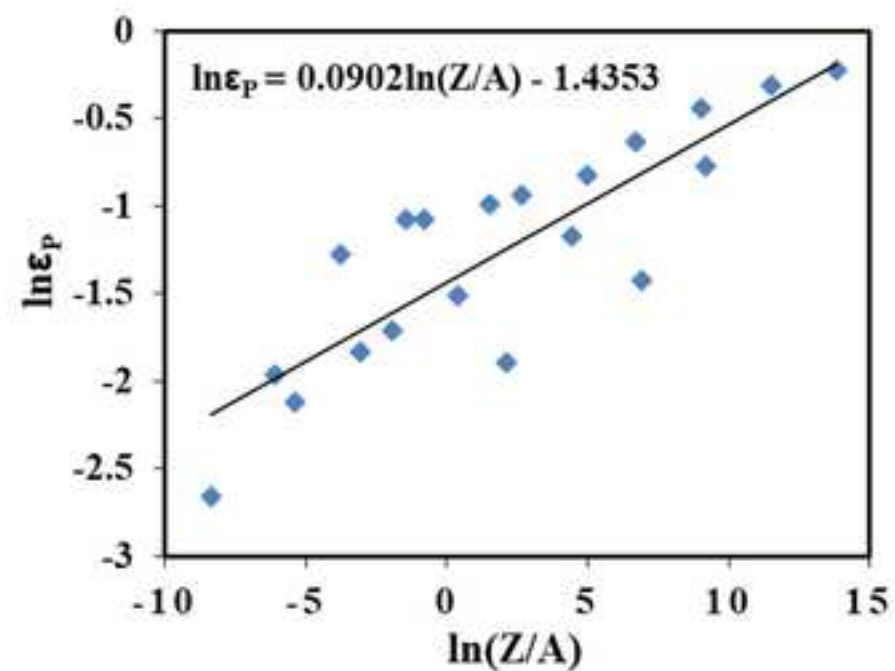
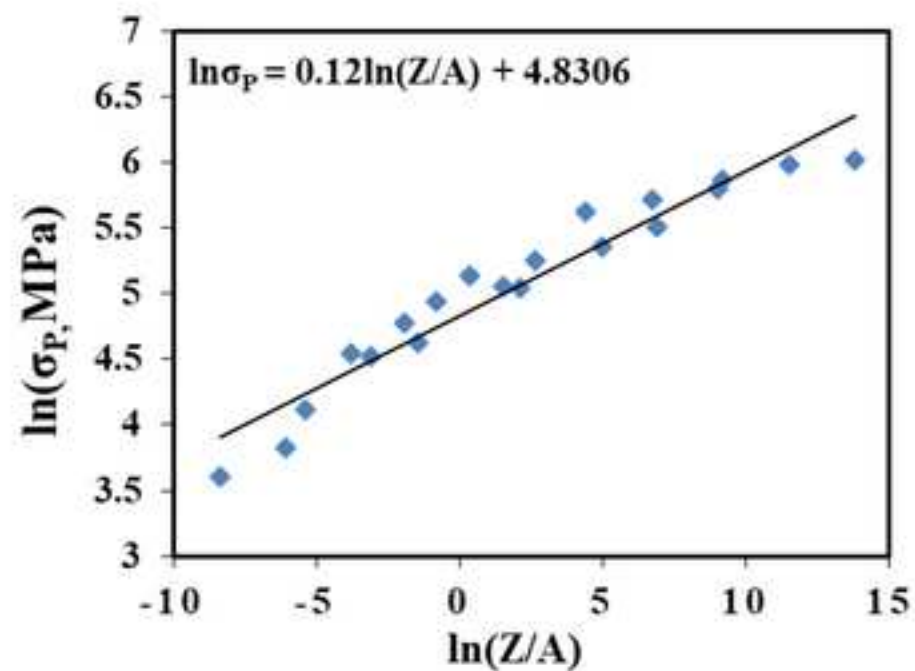












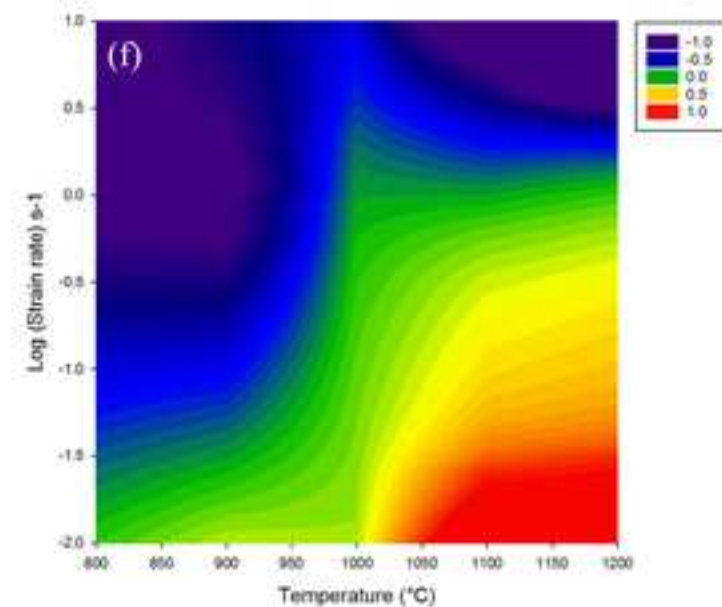
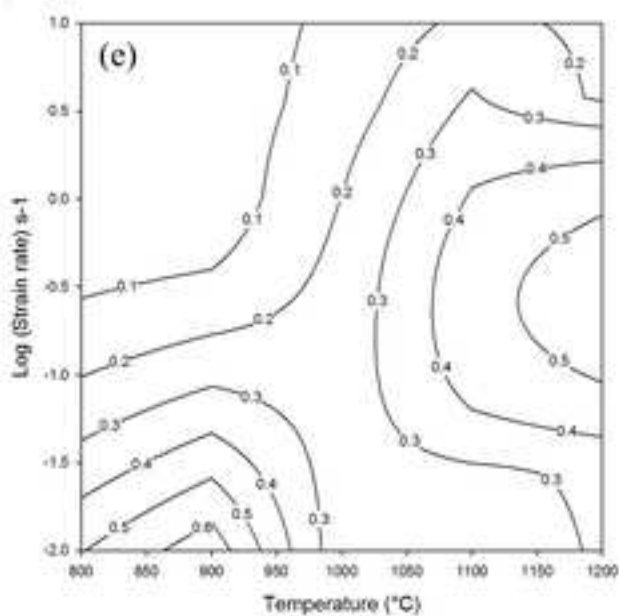
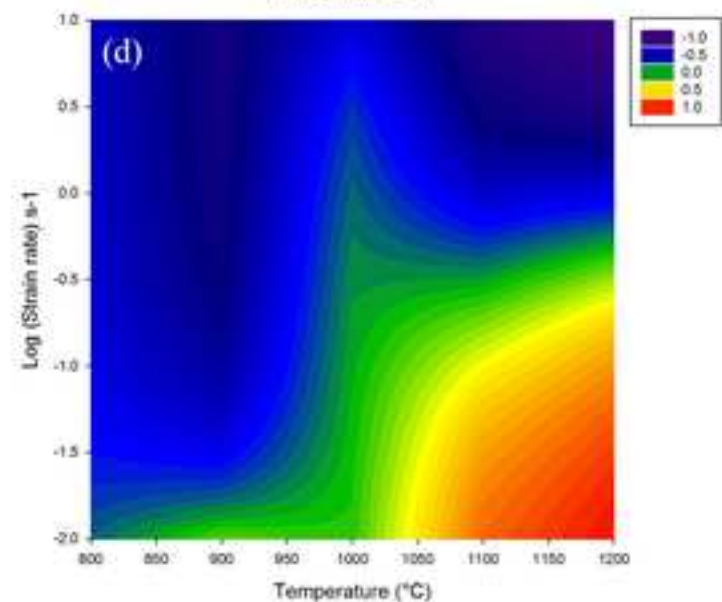
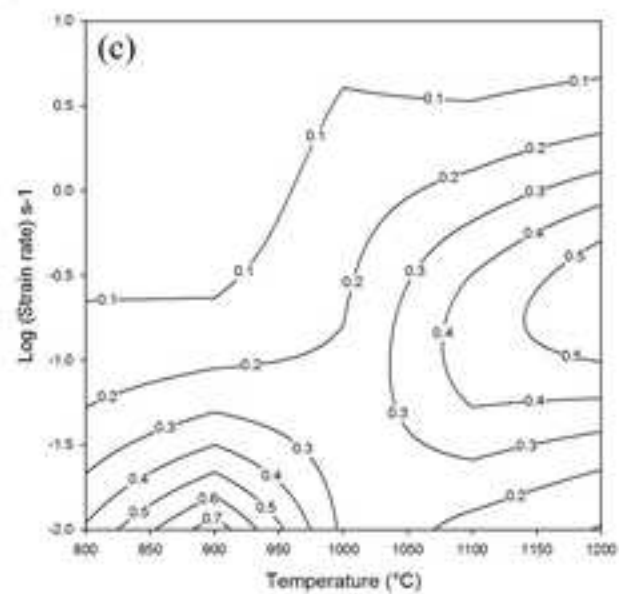
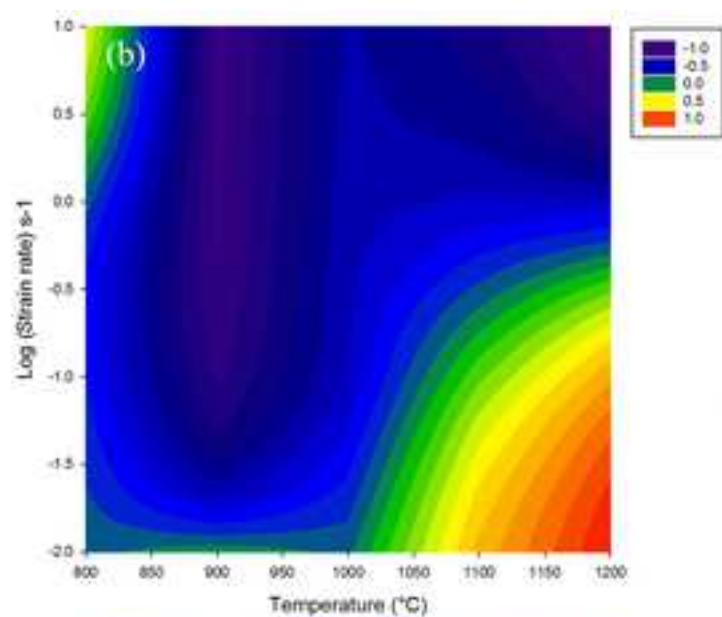
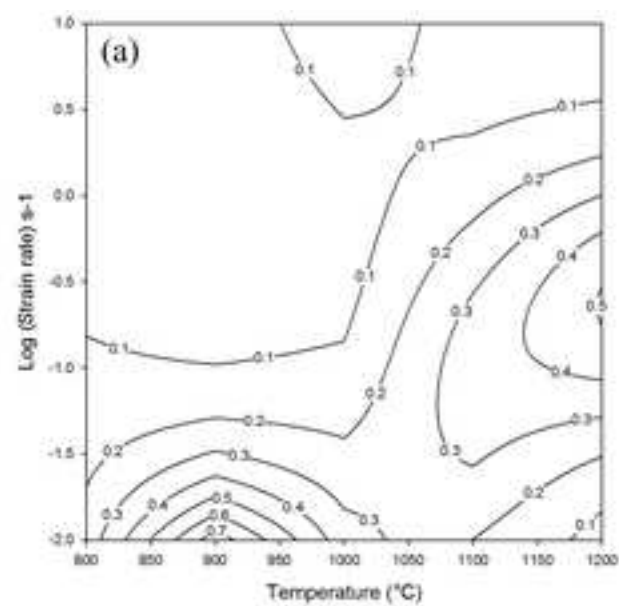


Figure 10

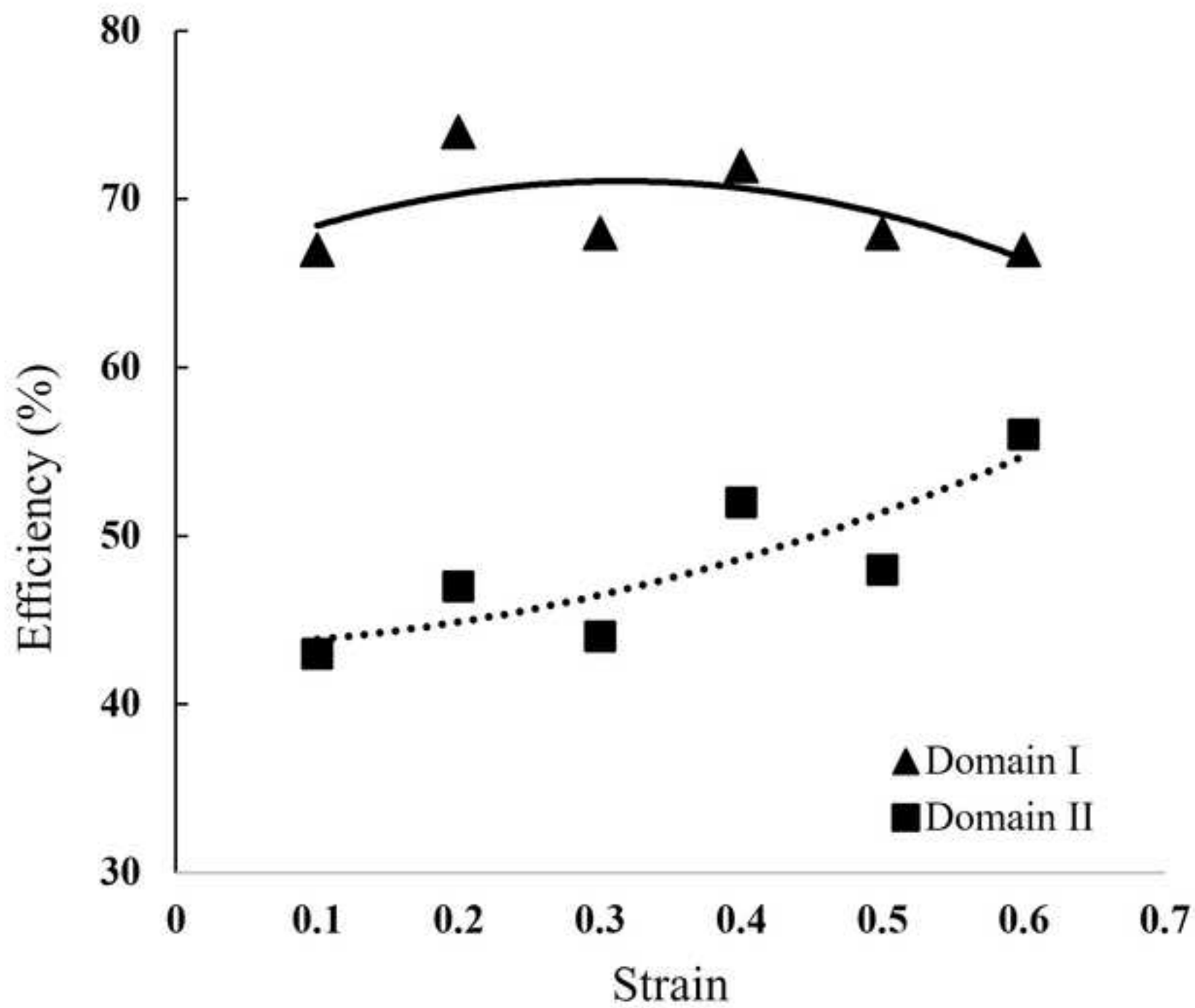
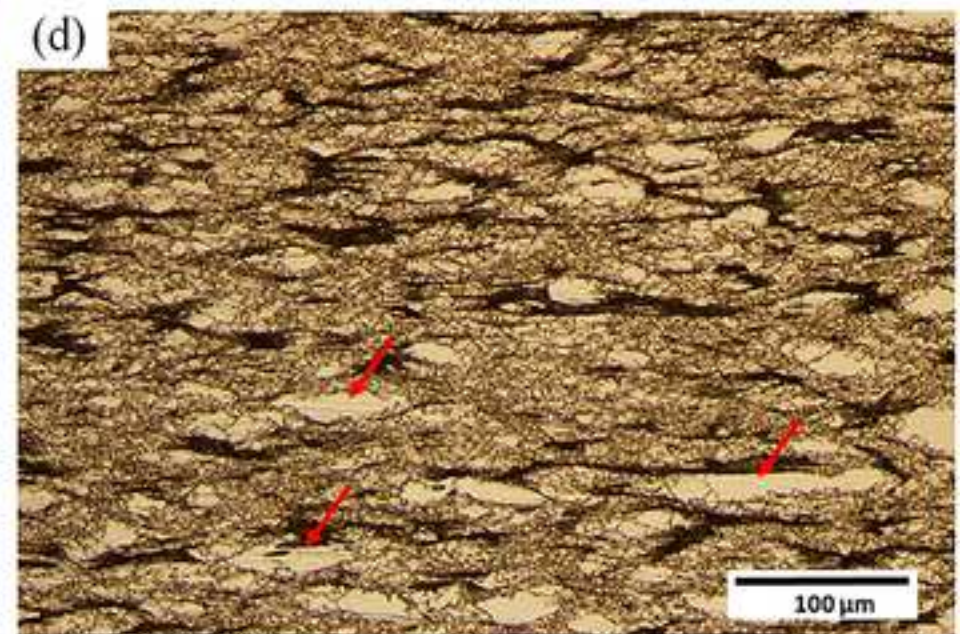
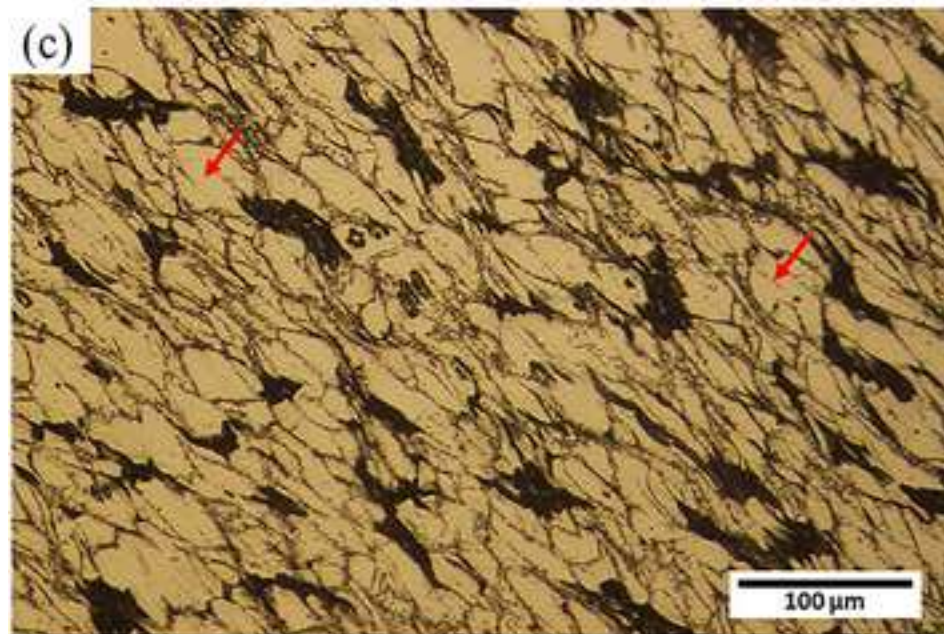
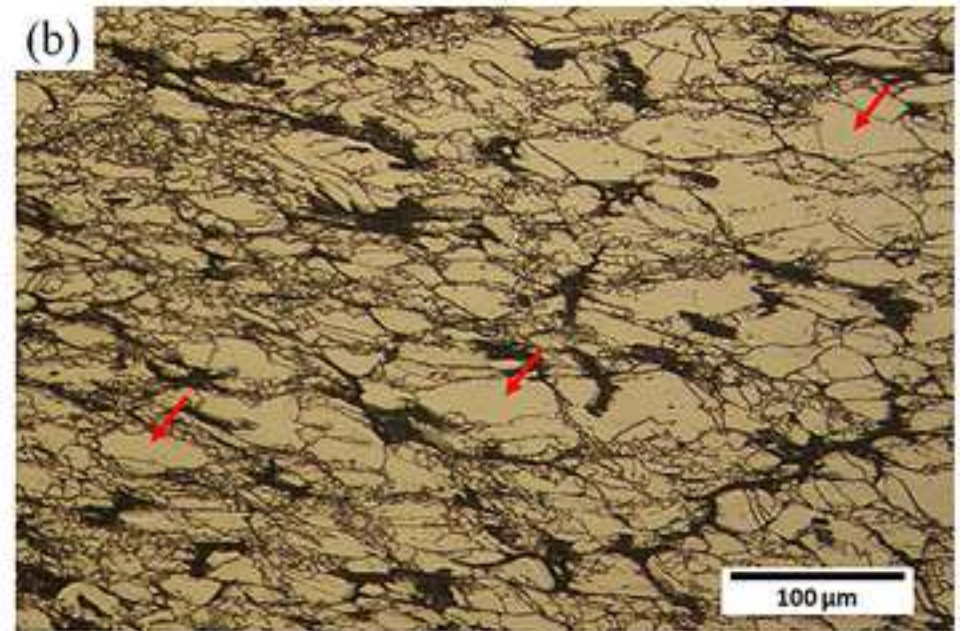
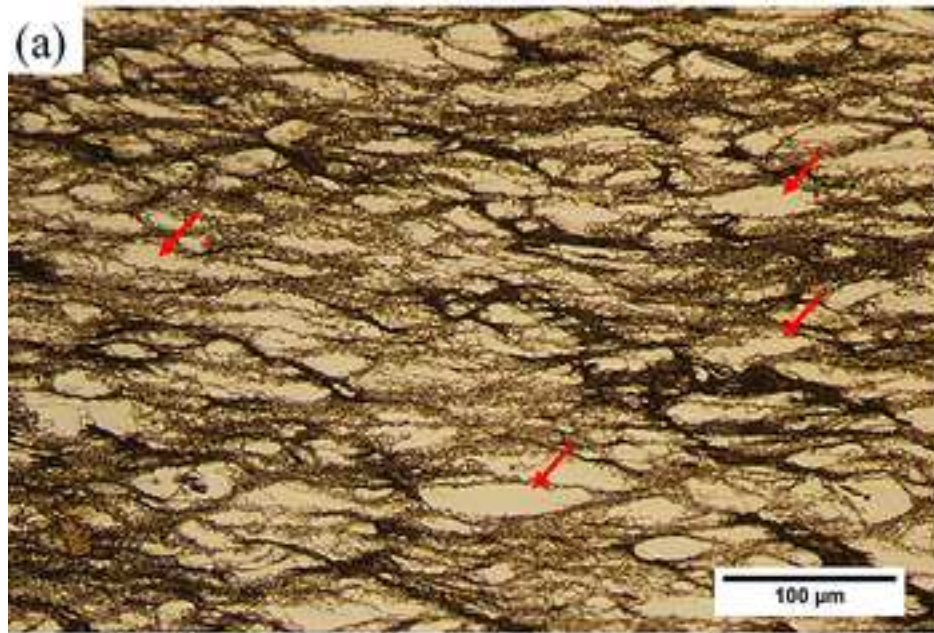


Figure 11



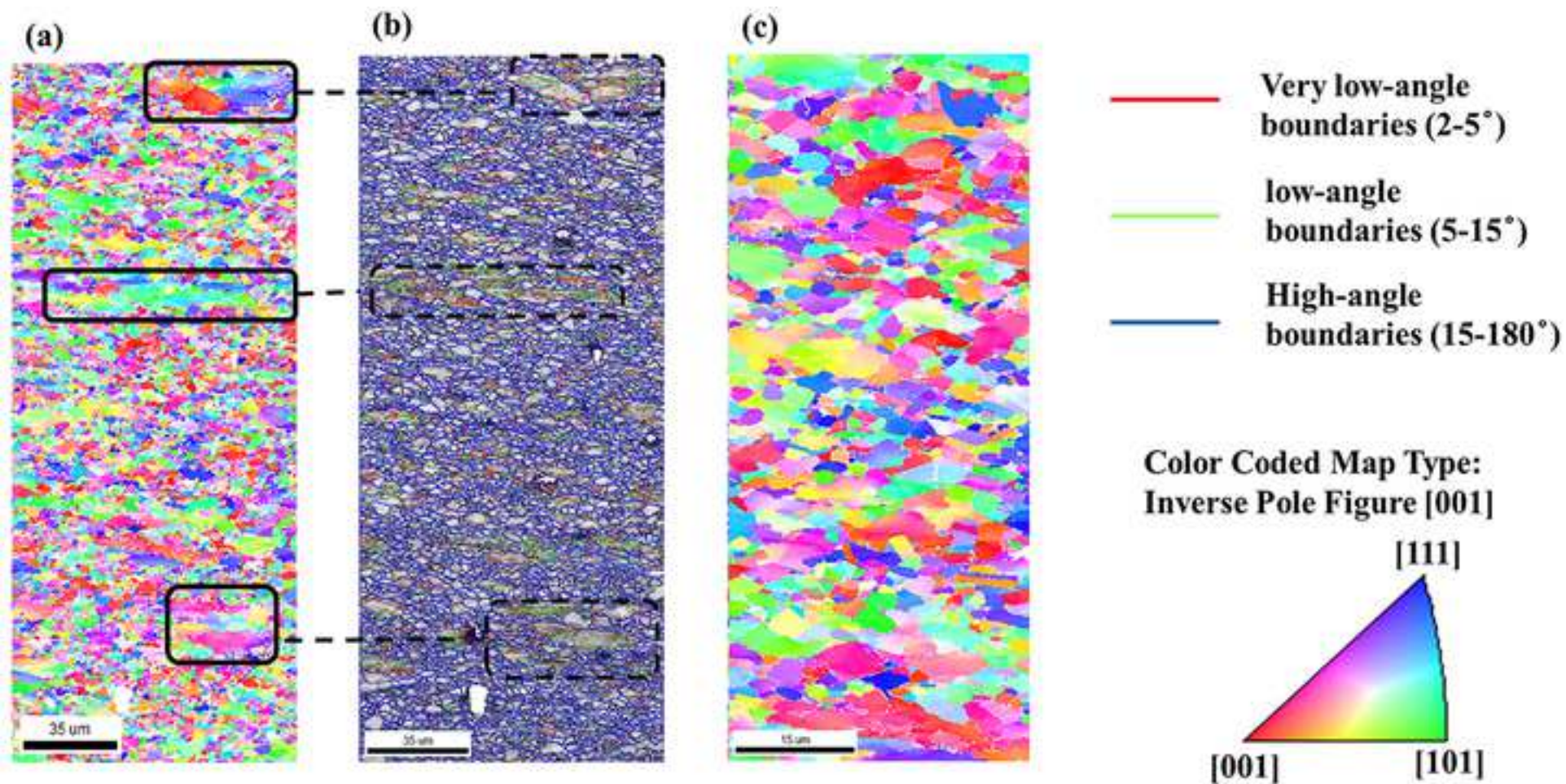
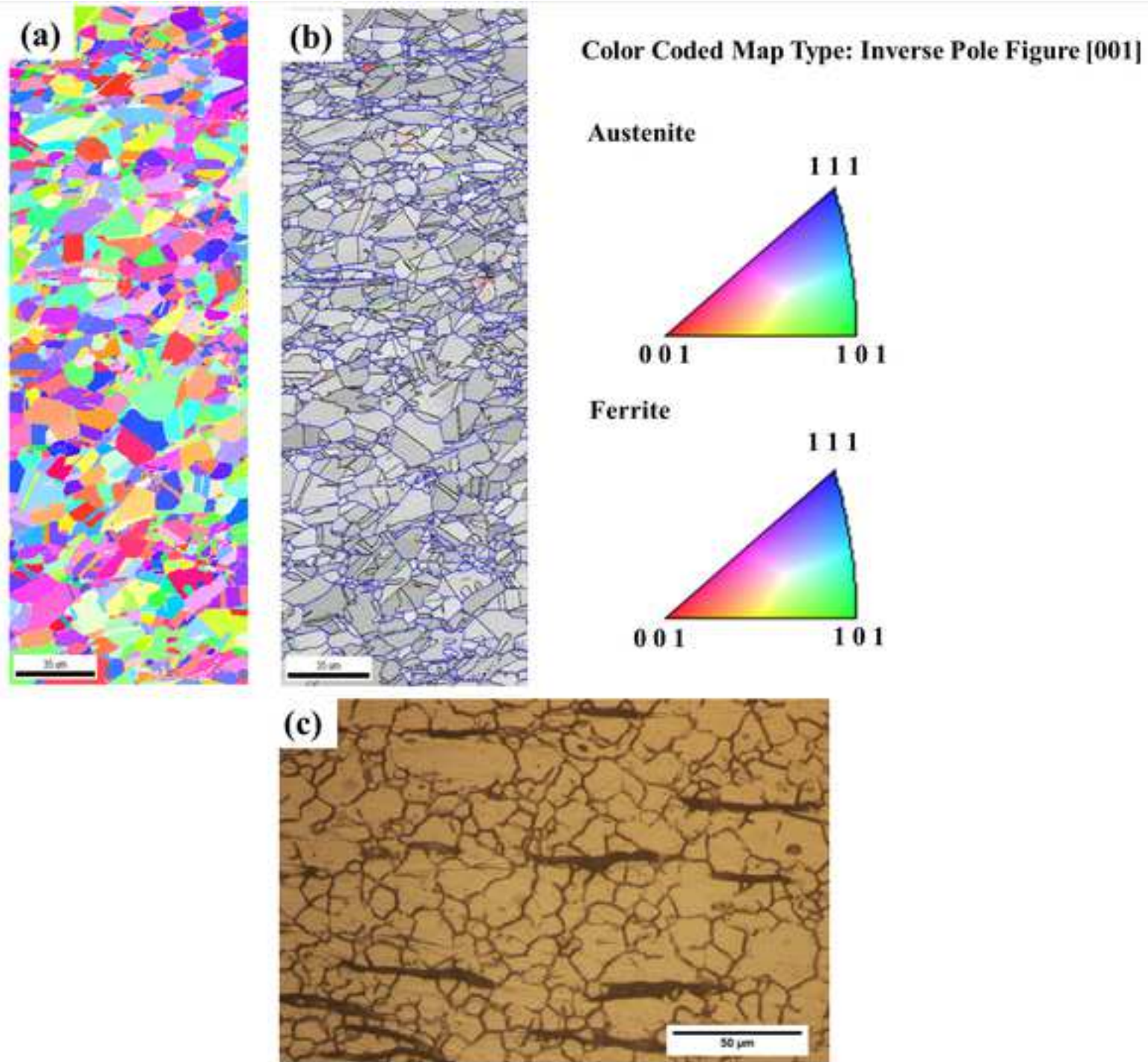
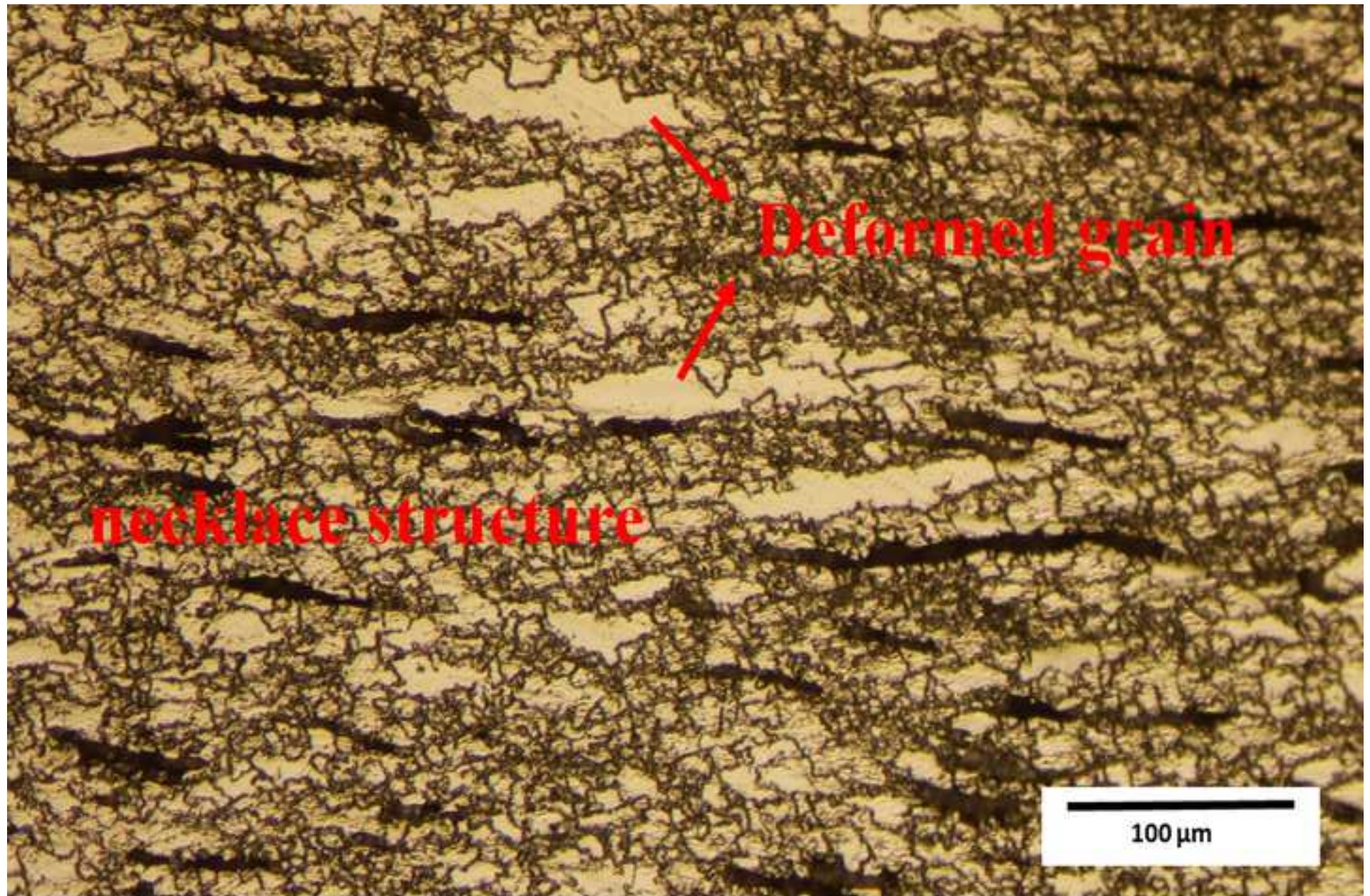


Figure 13





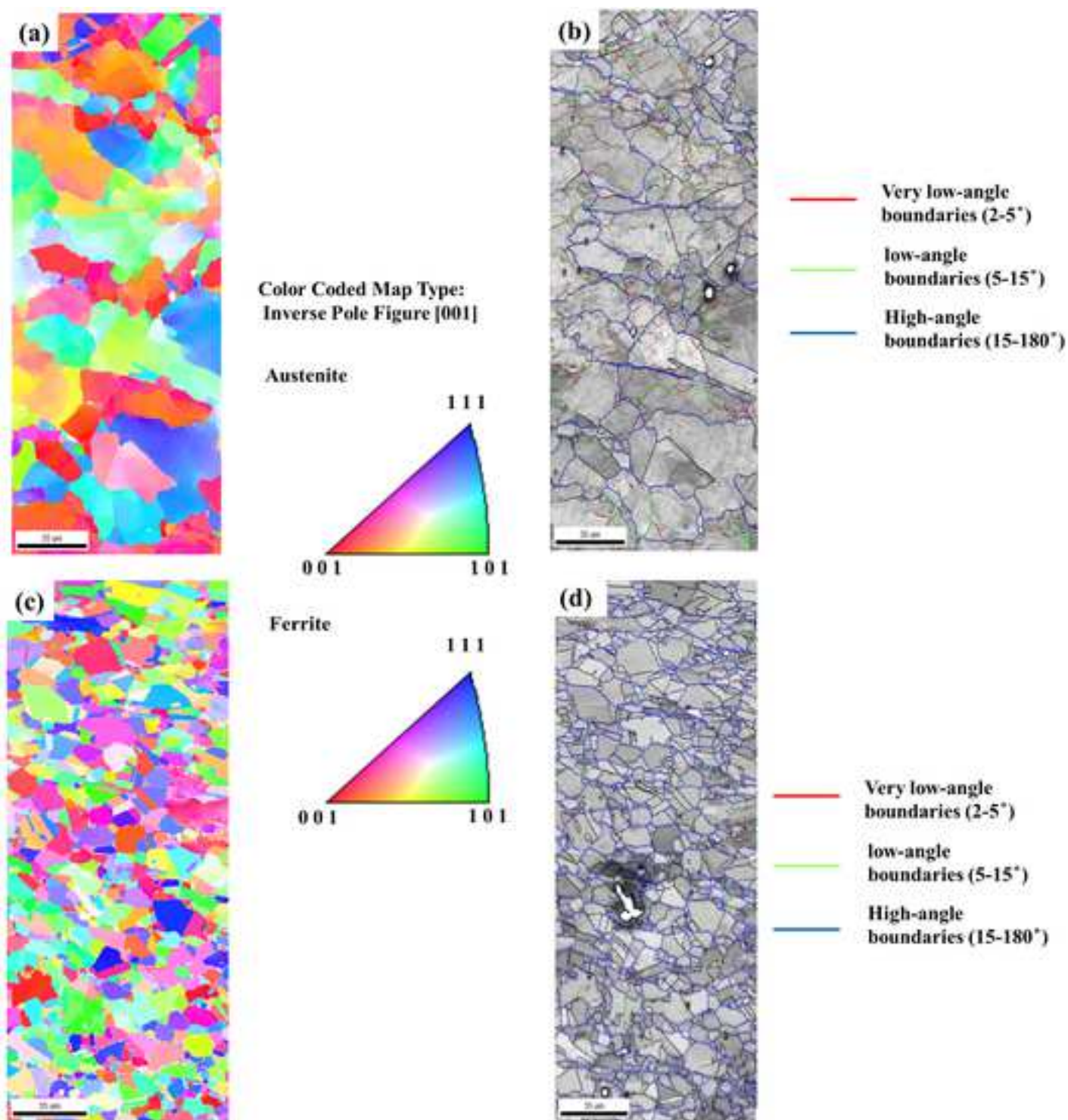


Figure 16

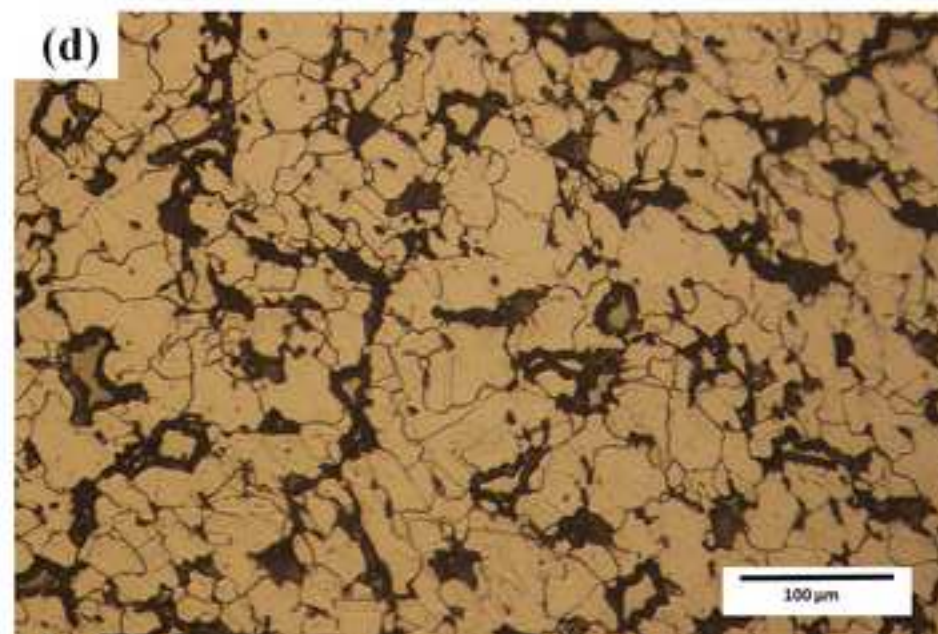
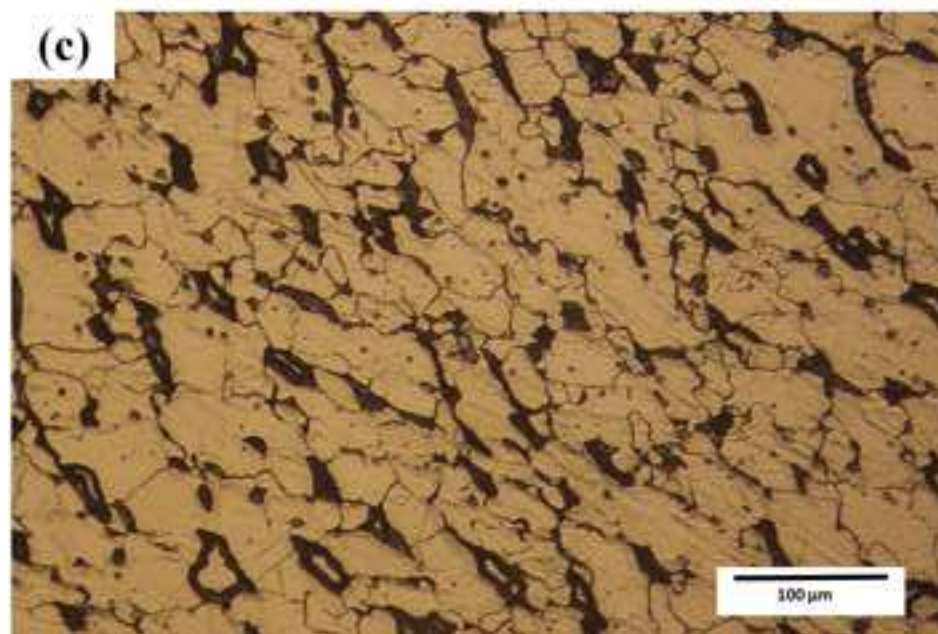
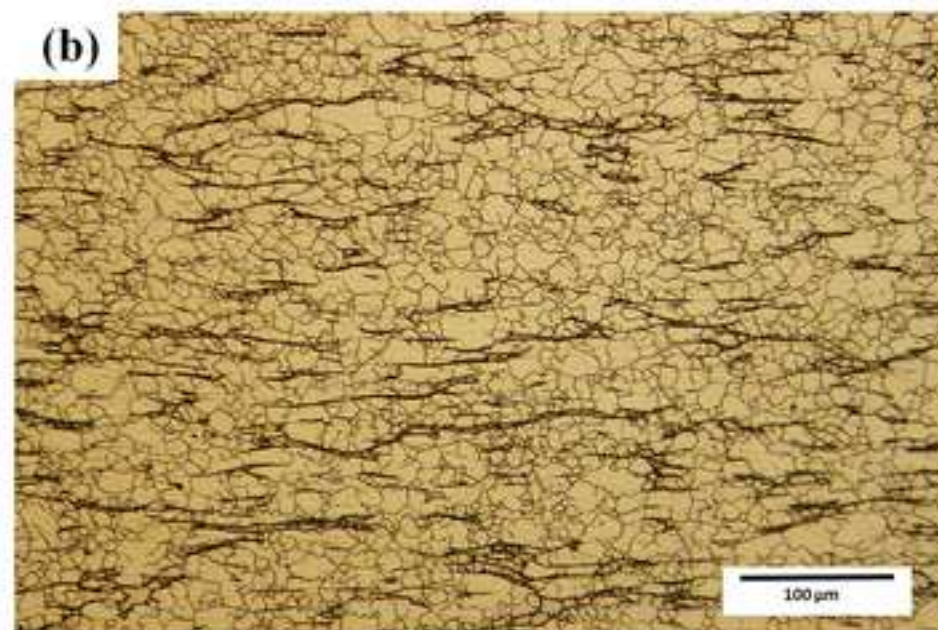
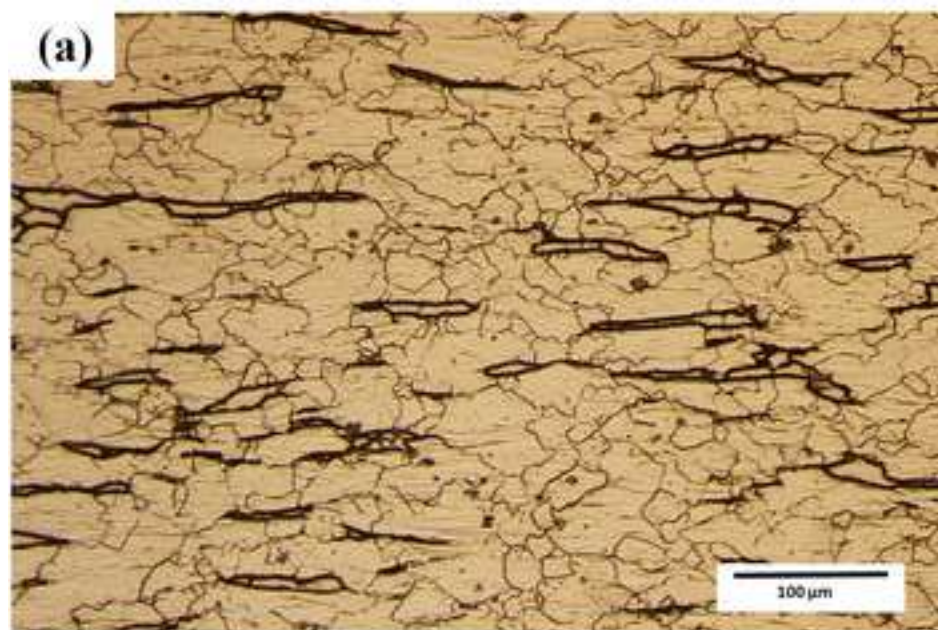
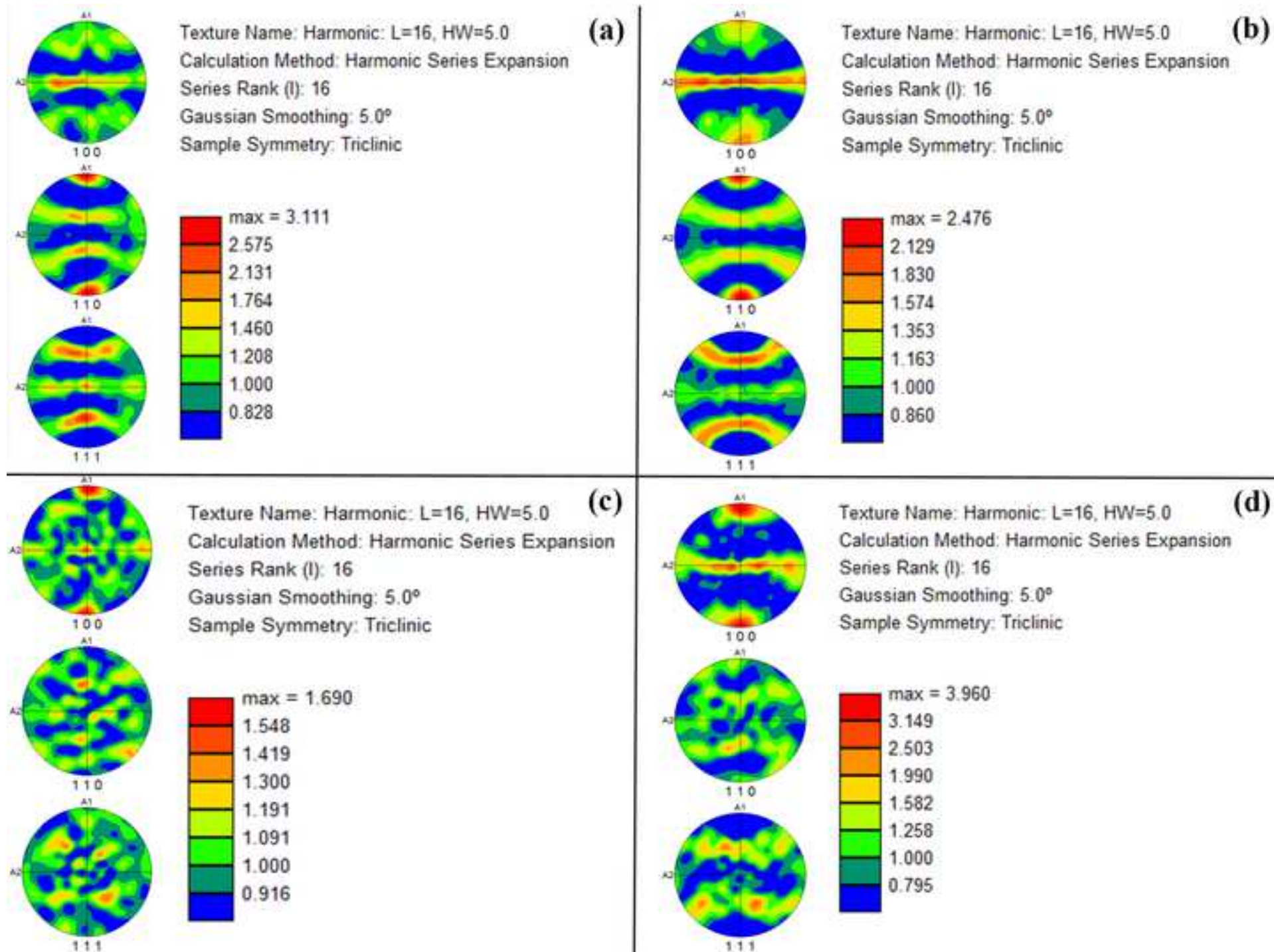


Figure 17



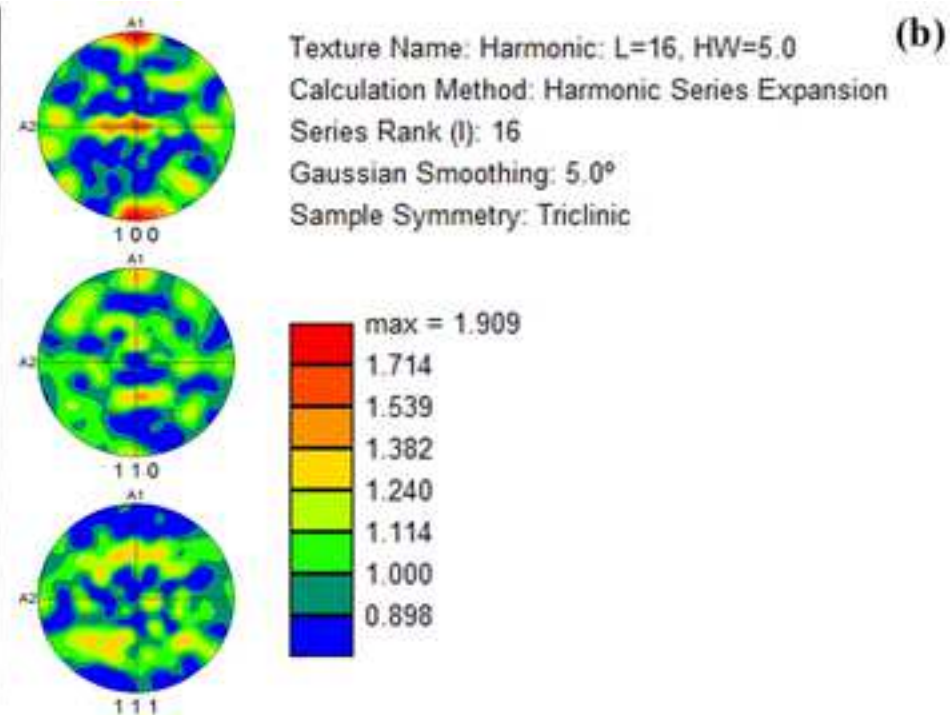
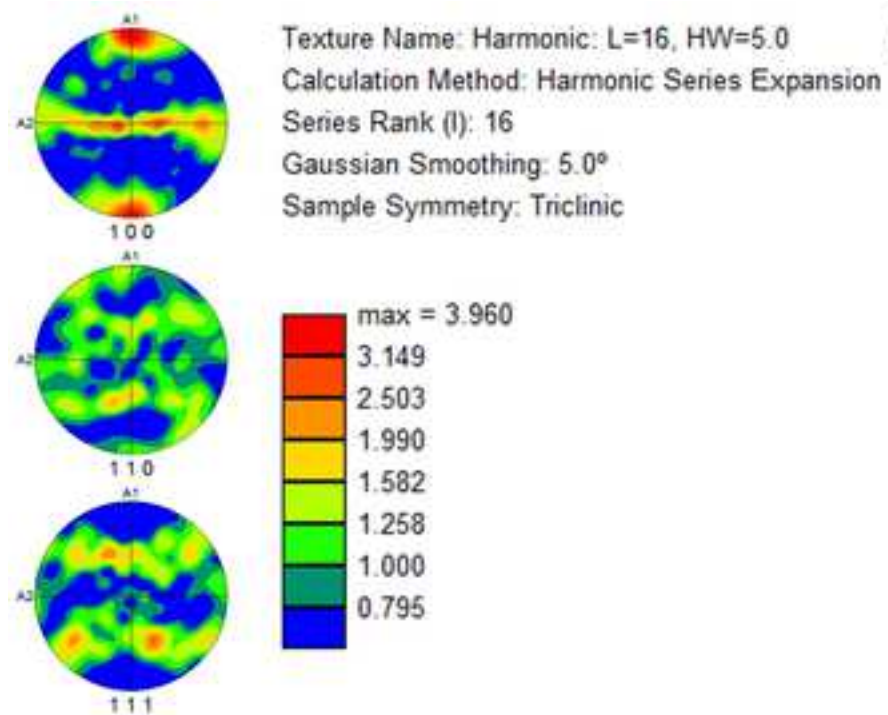
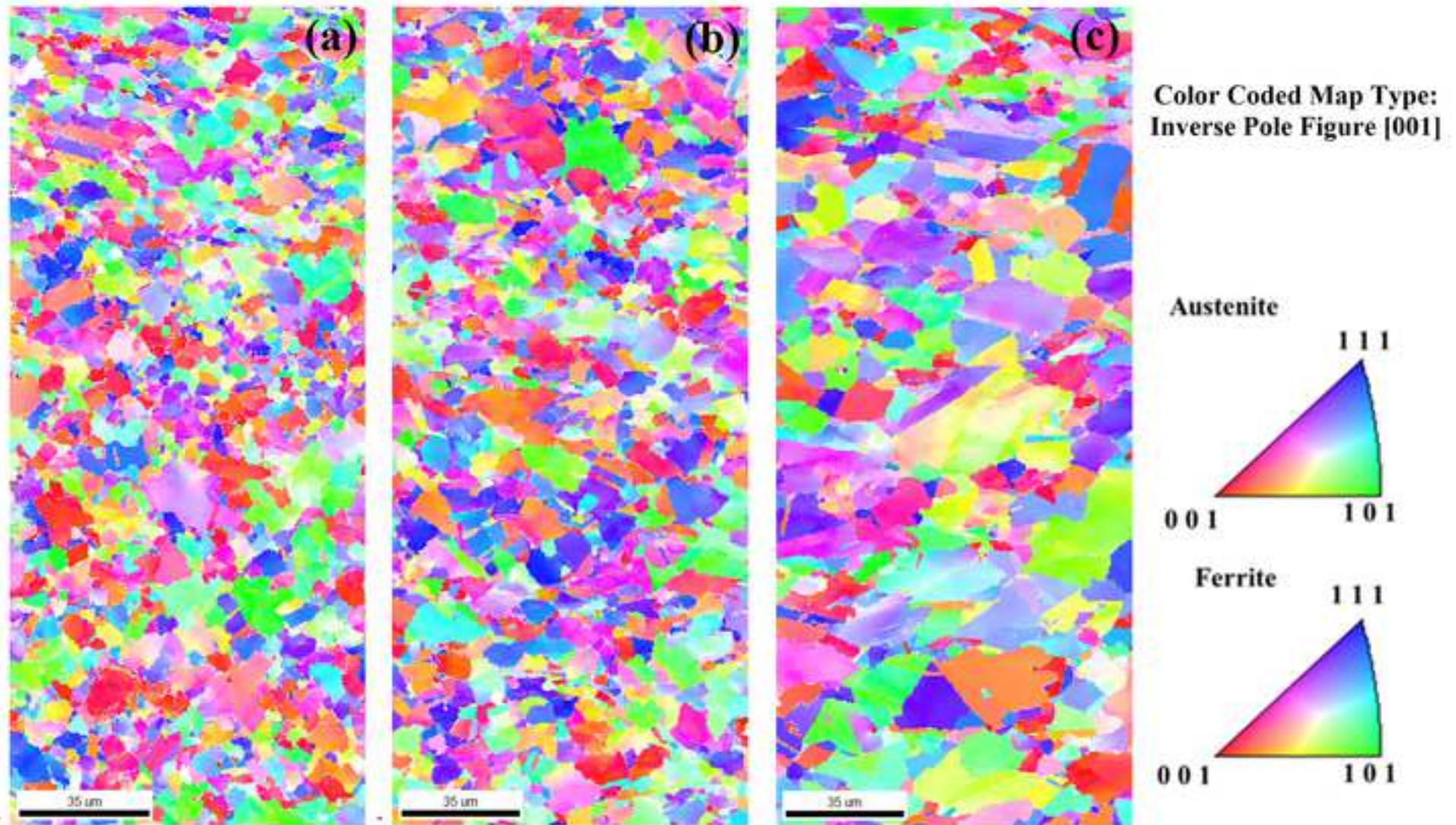
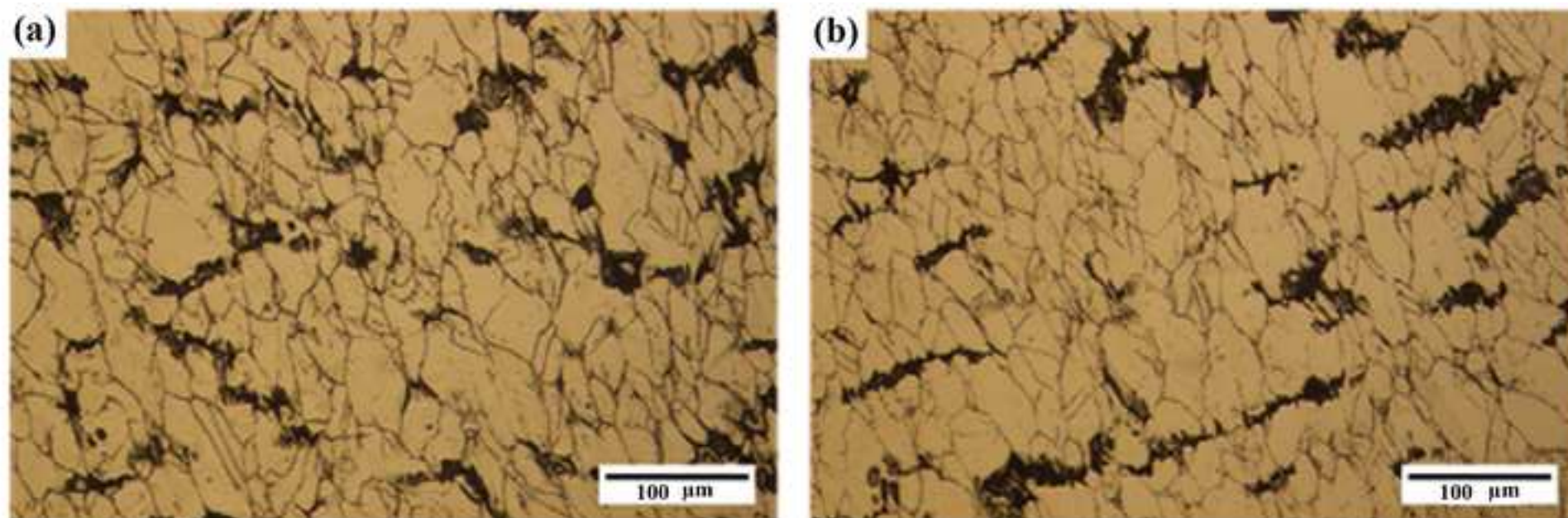
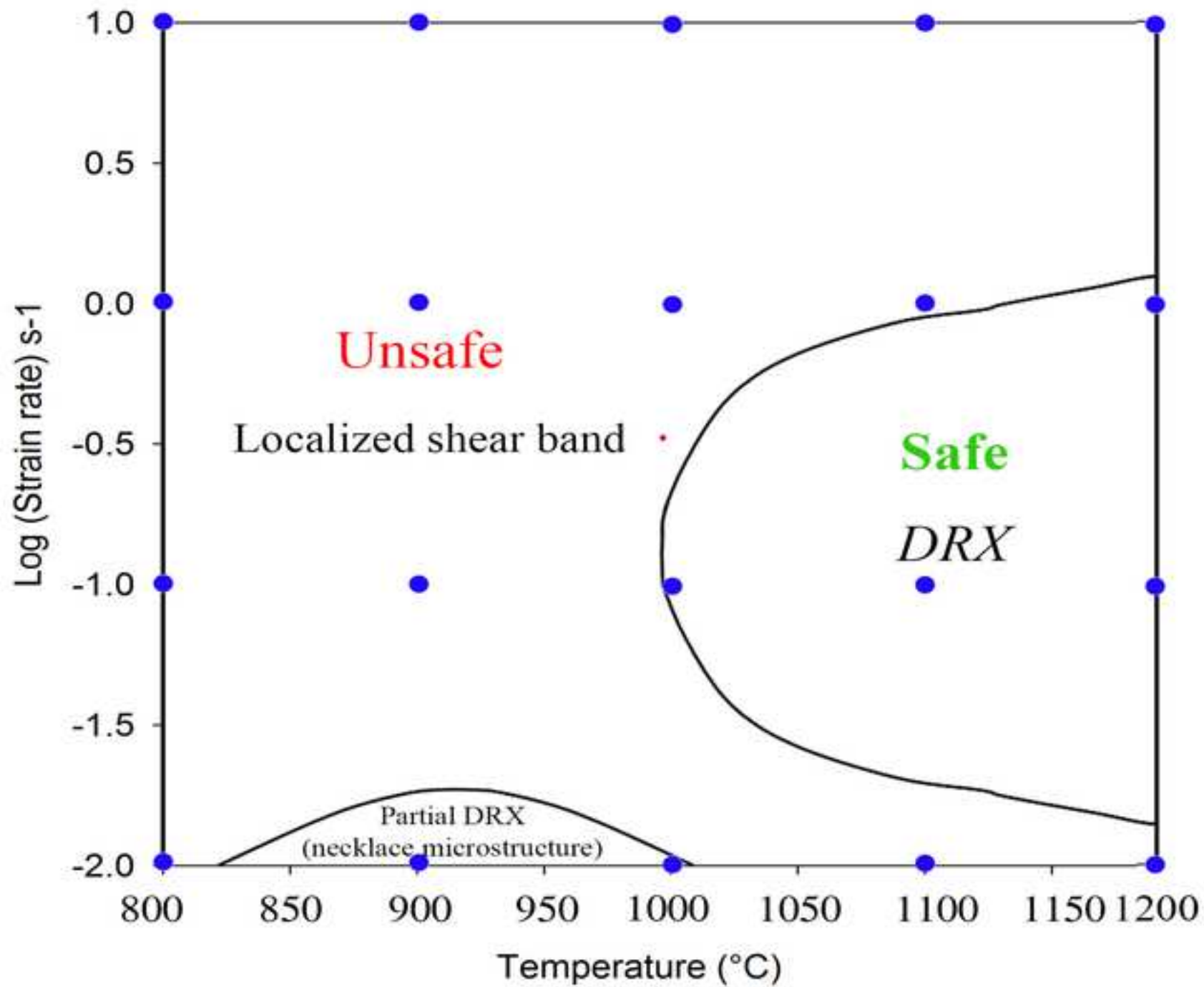


Figure 19







Declaration of interests

☒ The authors declare that they have no known competing financial interests or personal relationships that could have appeared to influence the work reported in this paper.

☐The authors declare the following financial interests/personal relationships which may be considered as potential competing interests:

Hossein Khorshidi: Investigation, Methodology, Writing- Original draft preparation,

Ahmad Kermanpur: Conceptualization, Supervision, Resources, Writing - Review & Editing

Habibollah Rastegari: Data Curation, Writing - Review & Editing

Ehsan Ghassemali: Investigation, Visualization

Mahesh C. Somani: Validation, Investigation, Writing - Review & Editing